



Experimental investigation of suddenly expanded flow at sonic and supersonic Mach numbers using semi-circular ribs: a comparative study between experimental, single layer, deep neural network (SLNN and DNN) models

Ambareen Khan^{1,a}, Parvathy Rajendran^{1,2,b}, Junior Sarjit Singh Sidhu^{1,c}, Mohsen Sharifpur^{3,4,d}

¹ School of Aerospace Engineering, Universiti Sains Malaysia, 14300 Nibong Tebal, Penang, Malaysia

² Faculty of Engineering & Computing, First City University College, Bandar Utama, 47800 Petaling Jaya, Selangor, Malaysia

³ Department of Mechanical and Aeronautical Engineering, University of Pretoria, Pretoria 0002, South Africa

⁴ Department of Medical Research, China Medical University Hospital, China Medical University, Taichung, Taiwan

Received: 11 March 2022 / Accepted: 2 March 2023

© The Author(s) 2023

Abstract In this work, we present the findings of the experimental study conducted in a rectangular duct at sonic and supersonic Mach numbers using passive control in the form of semi-circular ribs. Tests are conducted at sonic Mach number and four supersonic Mach numbers. The supersonic Mach numbers of the study are 1.5, 1.8, 2.2, and 2.5. The flow from the nozzles is discharged into the enlarged duct. The ribs are placed at 28 mm (1D), 56 mm (2D), 84 mm (3D), and 112 mm (4D) from the base to find the effect of the control mechanism on the flow field and the base pressure. The ribs of 6, 8, and 10 mm diameter are used to control the base pressure and ultimately the base drag. At Mach 2.2 and 2.5, control is not effective because the nozzles are over-expanded. These results reiterate the findings from the literature that the control is effective whether passive or active when nozzles flow under the influence of a favorable pressure gradient. The same is evident from the results at Mach 1.5 and 1.8. The NPRs at these Mach numbers are such that nozzles are under, correctly, and under expanded. When nozzles are operated for under expanded case, the control results in an increase in the base pressure when passive control is employed. These highly complex data are predicted using a single-layered neural network and a deep-layer neural network to save time and make it cost-effective, which shows that the data can be predicted with an accuracy of 0.88–0.99. The proposed models can predict the highly sensitive pressure terms for aerodynamic flows.

List of symbols

API	Application program interface
ANN	Artificial neural network
CFD	Computational fluid dynamics
CD	Converging–diverging nozzle
DNN	Deep neural network
DAQ	Data acquisition system
DOE	Design of experiments
<i>D</i>	Side of the square duct
<i>D</i> _i	Nozzle inlet diameter
<i>D</i> _{th}	Nozzle throat diameter
JBT	Jet boat tail
LES	Large eddy simulation
<i>L</i> _c	Nozzle converging length
<i>L</i> _d	Nozzle diverging length
<i>L</i>	Duct length
MTD	Mean Poisson, gamma, and Tweedie deviances
MAE	Mean absolute error

^a e-mail: khanambareen5@gmail.com

^b e-mail: aeparvathy@usm.my (corresponding author)

^c e-mail: sarjitsidhu@usm.my

^d e-mail: mohsen.sharifpur@up.ac.za (corresponding author)

MeAE	Median absolute error
MSE	Mean squared error
M	Mach number
NOC	No control
NPR	Nozzle pressure ratio
NN	Neural network
P_w	Wall pressure
P_w/P_a	Non-dimensional wall pressure
P_b	Base pressure
P_b/P_a	Non-dimensional base pressure
P_a	Atmospheric pressure
P_0	Stagnation pressure
SLNN	Single layer neural network
WC	With control
X/L	Non-dimensional location of the wall pressure taps on the duct
X	Location of the wall pressure taps on the duct
Θ_c	Nozzle converging angle
Θ_d	Nozzle diverging angle

1 Introduction

The subject of turbulent base flows continues to be an important field of study because of its significant influence on vehicle aerodynamic performance. Base flows are described as the separated recirculation flow due to a sudden increase in the base area. A separated flow in the base region gives rise to two undesirable issues: baseline inconsistency and a surge in drag. Base drag in certain instances contributes to as much as 60% of the overall drag. Many significant factors affect the flow's dynamics at the base, freestream Mach number, freestream conditions, the boundary layer before the separation, and the after-body geometry. Much research has been conducted by employing either active or passive control to reduce the base drag and increase vehicle performance. This study focuses on the effect of a semi-circular rib as a passive control in a square duct. The base pressure value is measured in an open jet facility. The obtained experimental results are normalized, processed, and analyzed. Later, the experimental results are analyzed by employing single-layered neural network (SLNN) and deep learning neural network (DNN) models.

The sudden expansion flow, which is a complex flow field, is shown in Fig. 1. It is seen that there is the boundary layer separation, a primary recirculation zone at the bottom corner, and a reattachment location at the wall. The passive control disrupts this flow field, increasing the base pressure and decreasing the base drag.

Figures 2 and 3 show the flow at a supersonic Mach number. When the flow is over-expanded, the oblique shock wave is formed at the nozzle exit, resulting in higher pressure values. An expansion fan is formed at the nozzle exit when the flow is under-expanded, resulting in a lower pressure due to the expansion of the flow and a longer reattachment length. Base pressure control plays a significant role in the minimization of base drag. The urge to control this has inspired many studies on abruptly extended flows [2–4]. Passive control techniques have always fascinated researchers since they provide expected outcomes without the requirement of any specific systems, as opposed to active control. There is considerable information available in the literature regarding abruptly enlarged flow problems, explaining the processes regulating the base flows [5–8]. Passive control generally employs geometric alterations like cavities and ribs to the expanded duct, modify the jet control to alter the shear layer's stability features, and function as flow control. Passive flow control management is usually more comfortable and hence more economical.

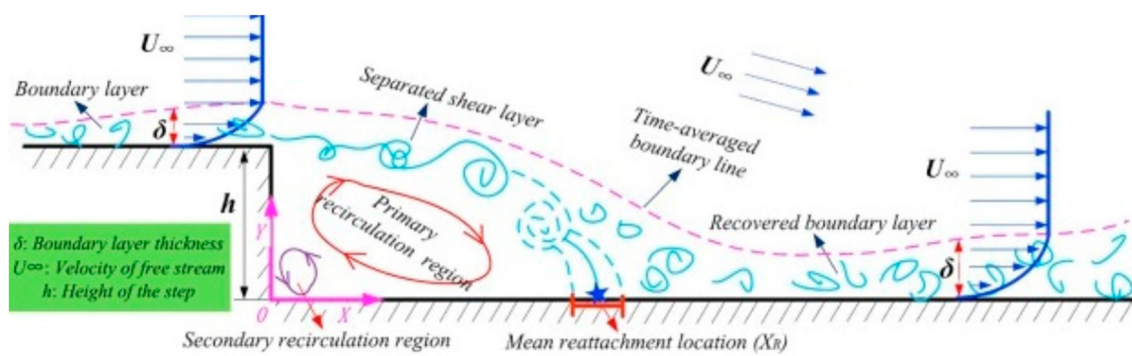


Fig. 1 Suddenly expanded flow [1]

Fig. 2 The over-expanded flow field in the C-D nozzle [1]

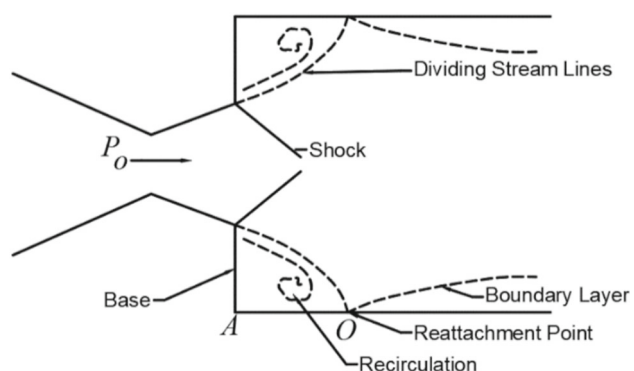
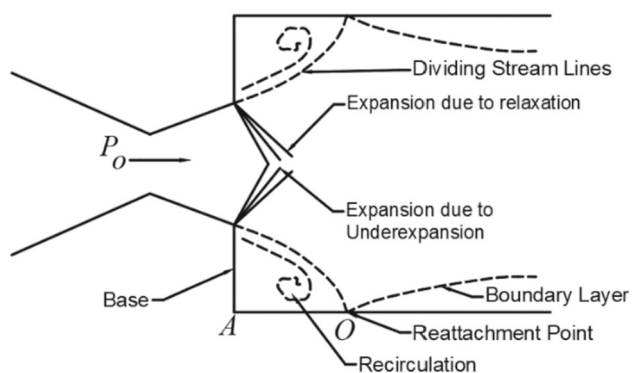


Fig. 3 Under-expanded flow through C-D nozzle [1]



Other passive methods include ribs, multistep vortex suppression, slotted cavities, dimples, spikes, etc. Among the most commonly used flow control methods for flow regulation in abruptly expanded flows are cavities (base and ventilated cavities), which could elevate base pressure based on system necessities. Anasu and Rathakrishnan [9] investigated the flow across an axisymmetric duct containing annular cavities placed at finite distances. They observed that the inclusion of additional cavity circulation decreases the oscillatory aspect of the flow in the expanded duct, allowing the flow to grow smoothly from the low pressure to the ambient pressure at which the jet was released. Consequently, the analysis was broadened by Rathakrishnan et al. [10] to cover several aspect ratios and reported that the cavity in the expanded duct has a significant impact and that the effect is more prominent for longer ducts than for shortened ducts.

The above studies mainly concentrated on subsonic flow. Vishwanath [11–13] carried out experimental studies using the base and ventilated cavities for sonic, transonic, and supersonic flow. They found a decrease in base drag up to 15–20% for base cavities operating at subsonic and transonic speeds, but this decrease is much lower at supersonic velocities. For ventilated cavities, the net reduction in drag was moderate because of viscous losses. Similar experiments were carried out by Pandey and Rathakrishnan [9, 14] for transonic and supersonic flows. They found a supplementary circulation to inhibit the oscillatory aspect of the flow because of cavities. This influence was more pronounced at subsonic Mach than in the supersonic flow regimes. They also found that the expanded area ratio significantly affects both the base pressure and flow development. The same observation was noted by Pathan et al. [15].

An experimental investigation was performed by Vikramaditya et al. [16] to explore the base cavity's impact on the pressure variations in the base section of a standard missile system at a transonic Mach number of 0.7. The analysis's main objective was to determine the variations in pressure and define the dominant mechanisms that drive them. They found that the base pressure variations features differ significantly across the azimuthal direction due to the model's asymmetric nature as the flow is highly non-uniform. They also found that due to the base cavity's inclusion, there is a sustainable improvement in the base pressure. Vigneshvaran et al. [17] carried out an experimental study on abruptly expanded duct flows of a higher area ratio. They found that the difference in base pressure progressively decreases with an increment in NPR. Wall pressure for a constant NPR displays continuous changes over the duct's length and exceeds ambient pressure at the duct's exit plane. They finally concluded that the cavity aspect ratio significantly impacted both the flow and base pressure. They also designed a cost-effective multi-channel data acquisition system (DAQ) and compared the results with and without control. Khan et al. [18] have reviewed various passive controls to reduce drag. Their study revealed that passive flow control is useful when a favorable pressure gradient is maintained at the nozzle exit. Vigneshvaran et al. [19] have reviewed ribs and cavities to control base pressure and wall pressure. He concluded that cavities act as a closed surface, and in the case of the rib, the minimum height should be maintained to avoid oscillations. Wall pressure is also essential when considering base pressure.

Rathakrishnan [20] analyzed the effects of annular ribs geometry, specifically, the aspect ratio on abruptly expanded axisymmetric flows, and found that it minimizes the base pressure compared to a duct in the absence of rib. Their experimental study concluded that the 3:1 aspect ratio of annular ribs proved to be more effective in reducing the base pressure for NPRs in the range from 1.41 to 2.58 at Mach $M = 1$. Besides, they do not cause any large oscillations in the duct's wall pressure field. In a similar study, Vijayaraja et al. [21] used rectangular ribs in the expanded duct and carried out experiments under subsonic and sonic conditions. They found that with the inclusion of ribs, base pressure decreases till an NPR of three. They concluded that ribs play a significant role in controlling base pressure. Vijayaraja et al. [22] studied the efficacy of annular ribs in base pressure regulation and examined the flow features for various Mach numbers for nozzles with abrupt expansion. They found that the aspect ratio plays a significant role in controlling the base pressure at subsonic and sonic flows.

Recently, dimples have been used as passive control devices to control the base pressure from an abruptly expanding convergent-divergent (CD) nozzle for a supersonic flow [23] and are more efficient at high NPR with smooth wall pressure. For further investigation, computational fluid dynamics (CFD) has also been used to simulate flow fields for a CD nozzle cavity [24]. Later, the effect of single and multiple cavities on the base pressure was also conducted [25]. The multistep vortex repression setup is another passive control technique originally suggested by Kidd [26] employing various layouts at transonic speed. At supersonic speeds, Viswanath [27] conducted wind tunnel tests using different multistep configurations. The last passive device is the streamwise slotted cavity, which Ibrahim and Filippone [28, 29] have computationally studied at transonic and supersonic velocities. But, because of the rise in viscous losses, this system has a negligible impact on the overall drag.

Two kinds of boat tailing are listed in the 2nd category of base drag mitigation techniques. The first kind is the conical (axisymmetric) layout that has two negative impacts on the transonic velocity projectile [30, 31]. One is the production of high Magnus force. The second is the natural shock wave production across the boat-tail. The non-axisymmetric layouts described by Agnone et al. [32, 33] are the second form. These layouts are square, triangular, and cruciform. Their analysis demonstrated that, among others, the triangular structure has greater ballistic efficiency.

Elawwad et al. [34] performed a numerical simulation of the flow through a triangular boat tailed projectile. They found a single normal shock wave hitting the shell at transonic speeds, which splattered at supersonic velocities. The wake area beyond the triangular base decreased, and the rear stagnation point shifted closer to the projectile base, hence reducing the base drag. Yunchao et al. [35] performed a numerical simulation using LES to minimize the base drag using a passive Jet Boat-Tail (GBT) flow control mechanism for automotive applications. The simulation results indicated that for passive flow jet increases the flow array combined with the primary flow and passes energy to the base flow by raising the base pressure, hence decreasing the base drag.

The experimental study was performed on microjets' efficacy to control the base pressure in a CD nozzle with sudden expansion [36, 37]. Another set of experiments was conducted to investigate the base pressure in high-speed flows at the design NPR with L/D ratios from 10 to 1 for various area ratios [38]. Later, the parameters were optimized using Taguchi (DOE) technique to regulate the base pressure [39]. Pandey studied the disparity in average velocity patterns along the abscissa. The four micro jets are positioned at the designated Mach number, and Virendra Kumar [40] for CD nozzles with abrupt expansion determines the control process's impact. They found that the nozzle's static pressure is minimal where the flow rate is highest while the static pressure is highest in the gap between two nozzles.

Another study on base pressure regulation using active control techniques with microjets for unexpectedly extended flow in the supersonic region is a numerical investigation [41]. They observed that the microjets are effective in regulating the base pressure and reducing drag. In a similar study, Sethuraman and Khan [42] carried out experimental research to calculate the base pressure and wall pressure distribution in the expanded duct for different Mach number and area ratios. They observed that microjets could regulate the base pressure only for more significant Mach numbers and higher area ratios.

Kumar and Rathakrishnan [43] analyzed the mixing features of an elliptic jet issuing from a CD nozzle at Mach number 2. They used rectangular tabs positioned all along the major and minor axes to control the jet. They found adequate mixing for the tabs placed along the minor axis than those placed along the main axis, irrespective of nozzle pressure ratios. In a similar study with flat and arc tabs along the major and minor axis, the authors [44] found that in the case of flat tabs across the minor axis, at all the NPRs tested, the waves in the core remain weaker, and the core length duration appears to be smaller than the uncontrolled jet. The current work focuses on improving the base pressure by applying passive control to add a new study in this base pressure field. Passive control in the form of rectangular tabs for sonic Mach from the circular duct is reported, while most of the analysis is based on active jet control.

The role of jets and other passive devices in different aerodynamic flow analyses is reported, as previously discussed. However, focusing on the semi-circular ribs in a high-speed flow where the nozzle cross section is a square operating at Sonic and supersonic Mach numbers is not reported. The combination of experimental study and machine learning regressors' ability to predict this highly sensitive data is lagging. To address this gap, this work aims to combine the experimental study of pressure variations in a suddenly expanded square duct and explore different techniques to predict the pressure variations with and without control using the passive method. Passive control flow management by semi-circular ribs located at different positions and diameters improves the base pressure. This study focuses on the passive control's effectiveness of semi-circular ribs of varying diameter on base pressure, total pressure loss, and flow development in the duct. However, SLNN and DNN modeling using APIs is performed for the first time in this field. Sixteen ANN models are proposed based on the combinations of input and output.

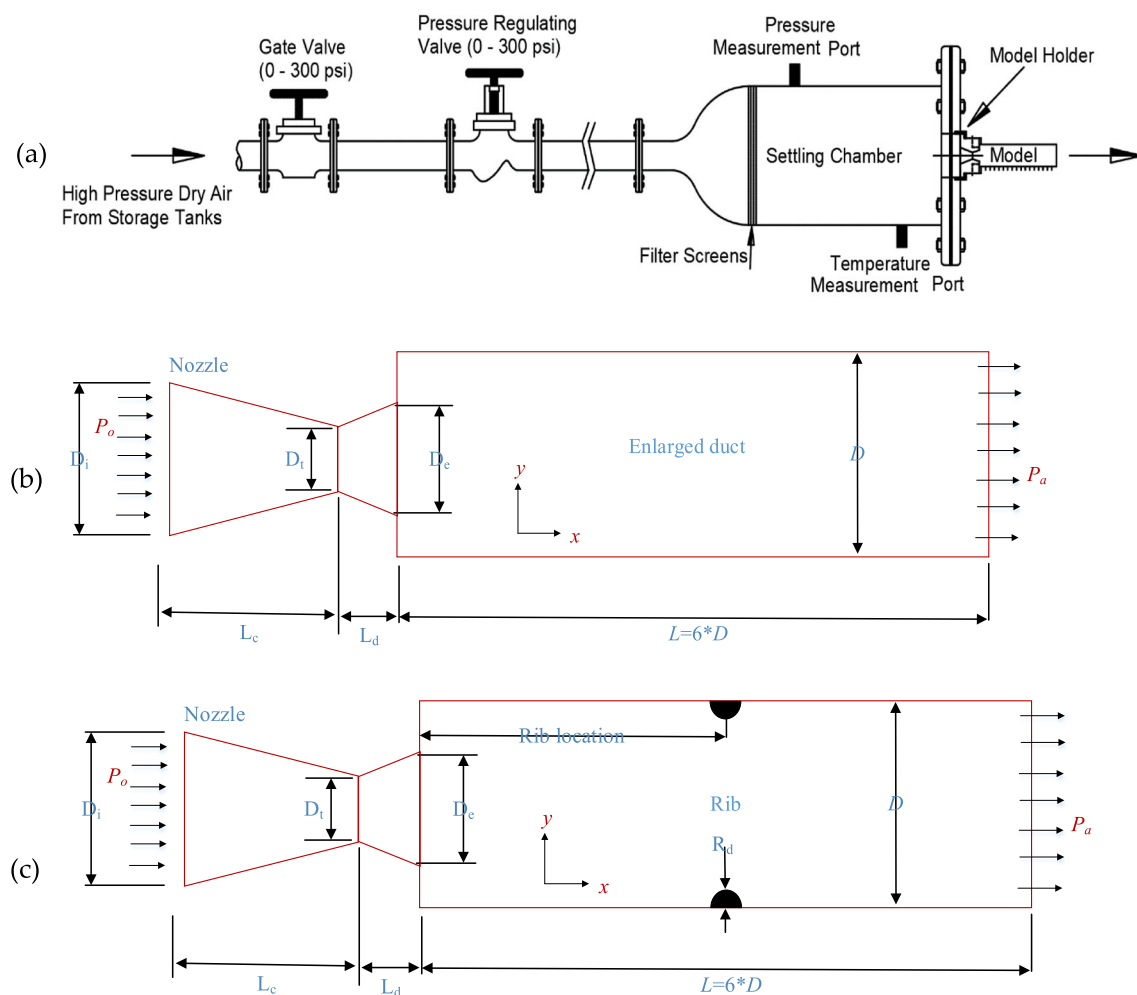


Fig. 4 **a** Experiment jet test setup **b** arrangement of nozzle and duct having no semi-circular rib (NOC) and having **c** semi-circular rib. Rib diameter (R_d) and its location are varied in case WC. D_i is nozzle inlet diameter; L_c is nozzle converging length, θ_c nozzle converging angle, D_{th} nozzle throat diameter, L_d nozzle diverging length, and θ_d nozzle diverging angle. Nozzle exit diameter was fixed at 10 mm

2 Methodology

Figure 4a displays the open jet facility setup used for the experiments. The reservoirs' pressure is transferred via a settling compartment equipped with flow conditioning units and expanded by a convergent and convergent-divergent nozzle of different dimensions depending on the Mach number. The overall temperature was identical to the local atmospheric temperature in the settling compartment. The jet in the research lab is ejected into the still surrounding atmosphere. A pressure transducer is used to measure the settling compartment stagnation pressure, base pressure, and wall pressure along the duct. The nozzle was attached to the settling compartment using the threaded coupling configuration, and air from the storage tank through the mixing length was passed to the settling compartment.

The settling compartment pressure P_0 was varied using the pressure control valve, and the regulating variable in this study (nozzle pressure ratio [NPR]) was kept fixed at the required levels. The still air from the settling compartment was allowed to expand via the nozzle to the enlarged square duct with 28 mm sides and 192 mm in length. In this study, the NPRs, which are the ratios of settling chamber pressure to atmospheric pressure, is varied from 1.5 to 10. The nozzle was fabricated from brass, and an extended square duct constitutes the experimental prototype shown in Fig. 4b. The duct in the nozzle outlet's downward direction is a straight wall to keep the recirculating area close to the base.

First, we select the Mach number and calculate the dimensions of the nozzle using isentropic relations. In our case, the exit diameter of the nozzle was maintained at 10 mm. These dimensions will be given for fabrication once the nozzle is fabricated. We calibrate the nozzle to find the exact Mach number at the exit of the nozzle. We can obtain the corresponding Mach number using Rayleigh supersonic pitot relay formula. Now, this calibrated Mach number is the actual Mach number at the exit of the nozzle, and the same is used for the experiment. During the nozzle calibration, the Mach number almost remains constant across

Table 1 Dimensions of the nozzle and duct making up the sonic and supersonic Mach flow

Flow type	Mach	All dimensions are in mm, and the angles are in degrees					
		D_i	L_c	θ_c	D_{th}	L_d	θ_d
Sonic	1	38	30	20	—	—	—
Supersonic	1.5	20.5	20	15	9.5	10.1	1.5
	1.8	22.34	25	15	8.34	9.51	5
	2.2	25.9	25	20	6.2	10.9	10
	2.5	24.4	25	20	6.15	10.9	10

the diameter of the nozzle exit, except near the surface. The flow in the duct is accelerated because the nozzle is converging and converging–diverging, and it gets separated when it exits the nozzle due to a sudden increase around the duct, and it flows to the end of the duct, where it reaches atmospheric pressure.

In the first case, the duct is kept clean (i.e., no disturbance to the flow field). It is the case with no control (NOC), as shown in Fig. 1b. When the semi-circular ribs are placed on the top and bottom walls of identical dimensions in the following case. This rib geometry is used to investigate the effect of ribs on the base pressure. It will be excited to investigate how it affects the turbulent flow at the base and controls the base pressure. These semi-circular ribs of 6, 8, and 10 mm diameter are not reported in the literature; hence, their effects will be studied. These ribs were placed at 1D (width/height of duct), 2D, 3D, and 4D away from the base corner, as shown in Fig. 1c. The mentioned position of 1D is chosen as the minimum position of the rib. A rib location less than this position will not affect base pressure as less than this position will be very near the base corner and will not be able to influence the base pressure in the duct. If the rib is placed beyond 4D, then it may be beyond the reattachment point. It will not be able to influence the flow field, and control will not be effective. 2D and 3D positions are considered for the rib as the reattachment point lies somewhere between the 3D and the 4D for a higher area ratio in most cases and will have maximum influence on base pressure. The semi-circular rib of three different sizes was considered to assess the impact of a passive control on the base pressure. Different ribs were machined to provide the following necessary aspect ratio after finishing all the testing with one aspect ratio (diameter) of the ribs.

The Mach numbers selected were low supersonic and high supersonic Mach numbers based on the literature survey. The study aims to assess the impact of the control mechanism at various Mach numbers and NPRs. The study is conducted for the first time using passive control in the form of semi-circular ribs, and the machine learning concept is applied.

In this analysis, three semi-circular ribs of 6, 8, and 10 mm are tested. The model area ratio, described as the duct cross-sectional area ratio to that of the nozzle outlet, and the length to diameter ratio of the expanded duct L/D are fixed at 7.84 and 10, respectively. The NPR, P_0/P_a (NPR), was the other variable of this analysis. The dimensions of the nozzles representing sonic and supersonic Mach numbers are provided in Table 1.

The flow is analyzed at sonic and four supersonic Mach numbers with and without control. The rib locations and their diameter are varied in the case of control, as previously mentioned. The calculations comprise the settling compartment's stagnation pressure, the base pressure, the pressure loss, and the duct's wall pressure distribution. The stagnation pressure at the duct's exit plane was also recorded by placing a pitot probe at the middle of the duct exit plane to evaluate the pressure loss. The wall pressure tapings are placed at equal intervals from the base corner to the duct outlet. These pressure tapings are provided to measure the flow's static wall pressure to analyze the rib's effect on the flow development and disturbances caused. All the measured parameters are repeatable within an uncertainty band of $\pm 3\%$. All measured pressures are normalized by dividing them by the ambient pressure. The wall pressure taps' locations are made dimensionless with the sides of the square duct D . The main objectives of this work are to control the base pressure, ensure smooth flow development in the duct, and reduce the overall pressure loss. Hence, the results are analyzed by considering all these characteristics.

2.1 ANN and DNN modeling

A neural network (NN) is a computational model that generates predictions based on knowledge from the past. An ANN consists of input sources that take inputs based on previously reported data. Backpropagation is carried out to maximize the neuron's weights to boost the NN's training. Lastly, the output layers are computed based on the input and hidden layer data. In ANN, a multi-layered network is called the backpropagation NN, which is the most widely used. It is also one of the most basic and standard techniques for training supervised NNs by altering and changing the nonlinear relationship between the input and the output.

The training/testing of the backpropagation network is in two stages. During the training process, the network is supplied with inputs and the necessary classifications. For instance, the input may be an encoded image of a face, and a code corresponding to the individual's name can explain the output. DNNs are an example of a single or multi-output regression problem algorithm. The numerous deep learning libraries are readily available to define and evaluate NN models for multi-output regression tasks. DNN is a network-based artificial neural approach consisting of hidden layers between the input and the output layers. DNN gathers and

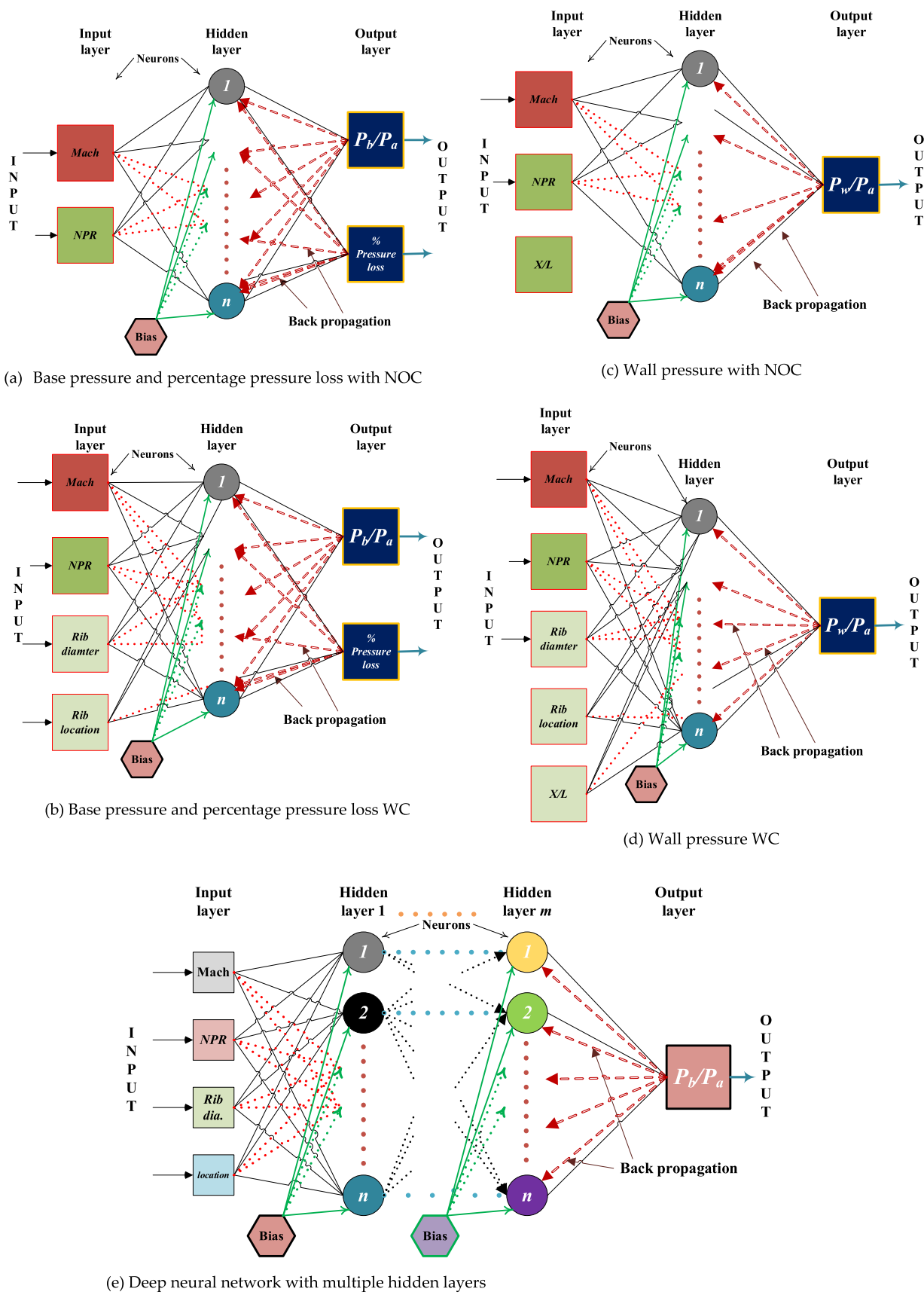


Fig. 5 Base pressure, % pressure loss, and wall pressure model using (a–d) SLNN and an illustration of (e) DNN for base pressure

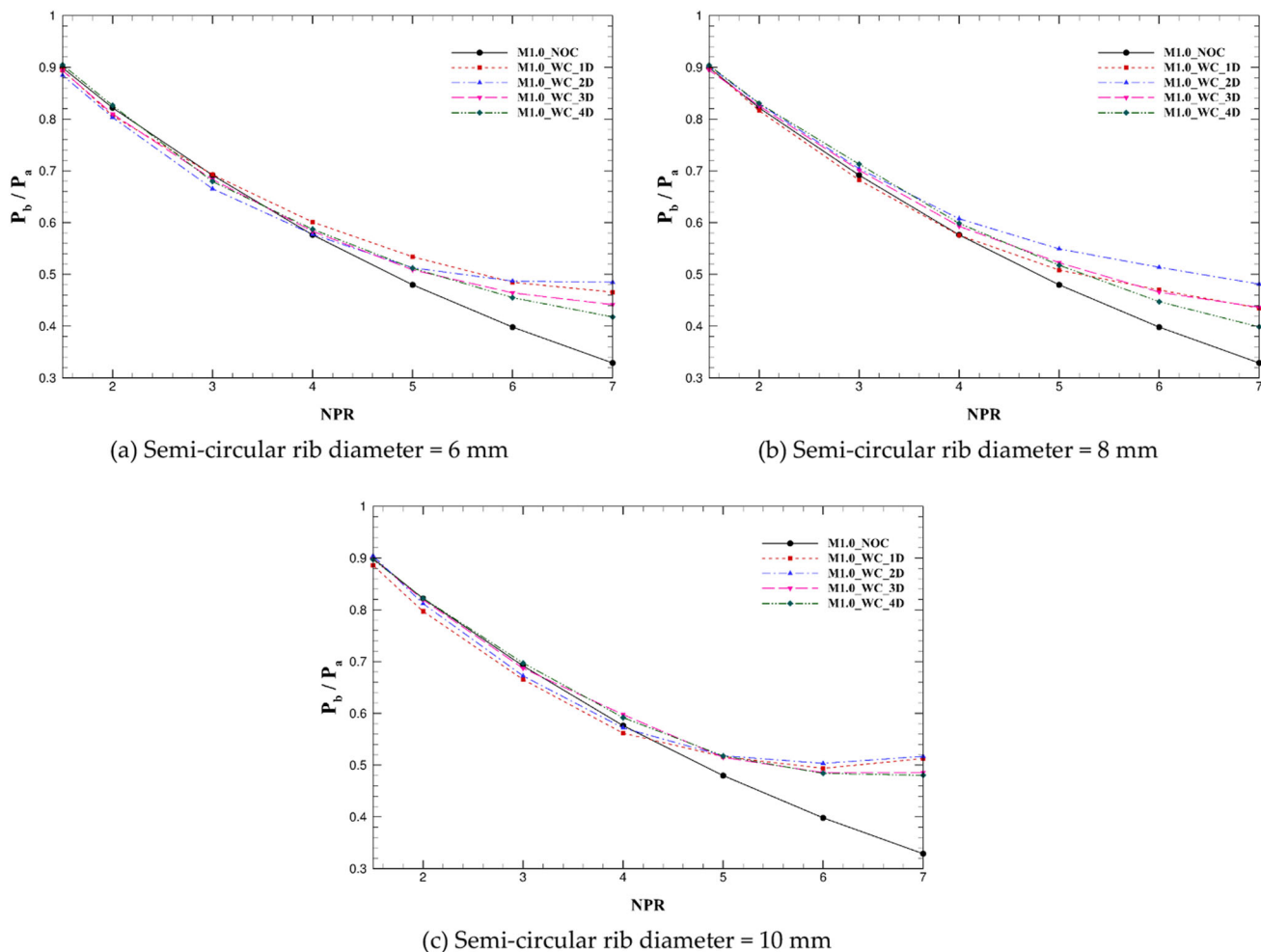


Fig. 6 Effect of semi-circular rib on the base pressure at sonic Mach number

generates high-level features from low-level features [45–47]. This feature allows the source to create high-level features. The input layer of a DNN takes raw data, and each subsequent hidden layer learns to convert the raw input data into an abstract representation of the raw data.

In this work, SLNN and DNN are used to model the base pressure, wall pressure, and percentage pressure loss. Four NN models are designed based on the number of inputs for these characters of high-speed flow. In SLNN, four models are shown having a single hidden layer, as shown in Fig. 2a–d.

The combinations of inputs and outputs are illustrated. The flow without a rib has only two input parameters, namely, Mach number and NPR, separately modeled with base pressure (P_b/P_a) and percentage pressure loss (Fig. 5a). The non-dimensional X/L gets added for wall pressure because it depends on the location of pressure tapings on the duct wall; hence, it is separately modeled (Fig. 5b). In the case of flow with rib, two more inputs are added: rib diameter and rib location. The respective outputs are modeled, as shown in Fig. 5c, d. The demonstration DNN model is shown in Fig. 5e, where the hidden layers are considerable [48–51]. Four DNN models, such as SLNN, are developed with the same input and output combinations.

The two major NN models developed are further tried using the Keras library, in which the sequential and functional application program interfaces (APIs) are used for the computations. The sequential and functional APIs of the SLNN and DNN models are mentioned in Algorithm 1. Hence, the total models developed are $2 \times 4 \times 2 = 16$ models in the experimental data of this study. More comprehensive network topology with 12, 8, 10, and 5 neurons in the hidden layer is adopted for numerical data regression. A vector of Mach, NPR, rib diameter, and rib position (more or less) is used for our proposed SLNN and DNN networks. Given that the feature vector is different in each data set, we transferred it to two fully connected layers with varying output sizes, each of which reduced the number of dimensions in the feature vector. These outputs can be considered a matrix multiplication for high-level input data abstraction.

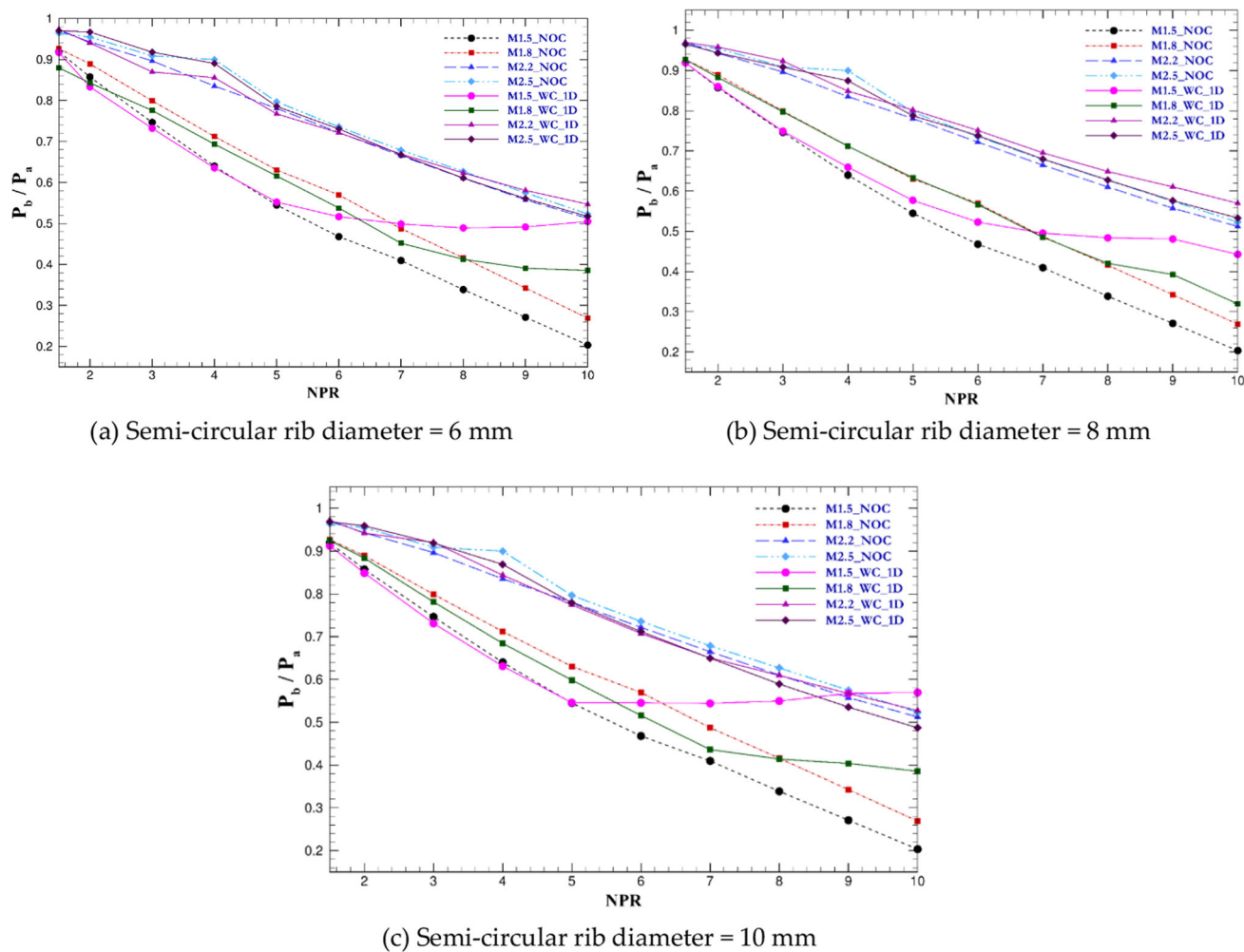


Fig. 7 Effect of semi-circular rib on base pressure at 1D at supersonic Mach number

Algorithm 1: SLNN/DNN model

Inputs: Mach, NPR, rib diameter, rib location, and X/L

Output: P_b/P_a , percentage pressure loss, and P_w/P_a

1. Feed input dimension, output dimension, number of hidden layers, and neurons/layer
2. Input data set
3. Split data set randomly for training and testing
4. Define the model as sequential
5. Add the first hidden layer with neurons/layer and input dimension
6. Add multiple hidden layers if the DNN model is required
7. Add the output layer with output dimension and activation function
8. Compile the model selecting “adam” as an optimizer and MSE as loss metrics
9. Fit the model for training with 200 epochs, validation split = 0.33, and batch size = 10
10. Predict the output using the trained model for the test data set
11. Compute the performance metrics

2.2 Performance evaluation

As previously mentioned, the following performance metrics are used to assess the accuracy and loss of the developed SLNN and DNN models for various input and output combinations. These metrics are computed to gauge the performance of our models. They explain how appropriately the model is subjective rather than objective. The gradient descent is calculated using different metrics as cost functions. The variance of the input variables can be understood and explained using these metrics [51–54].

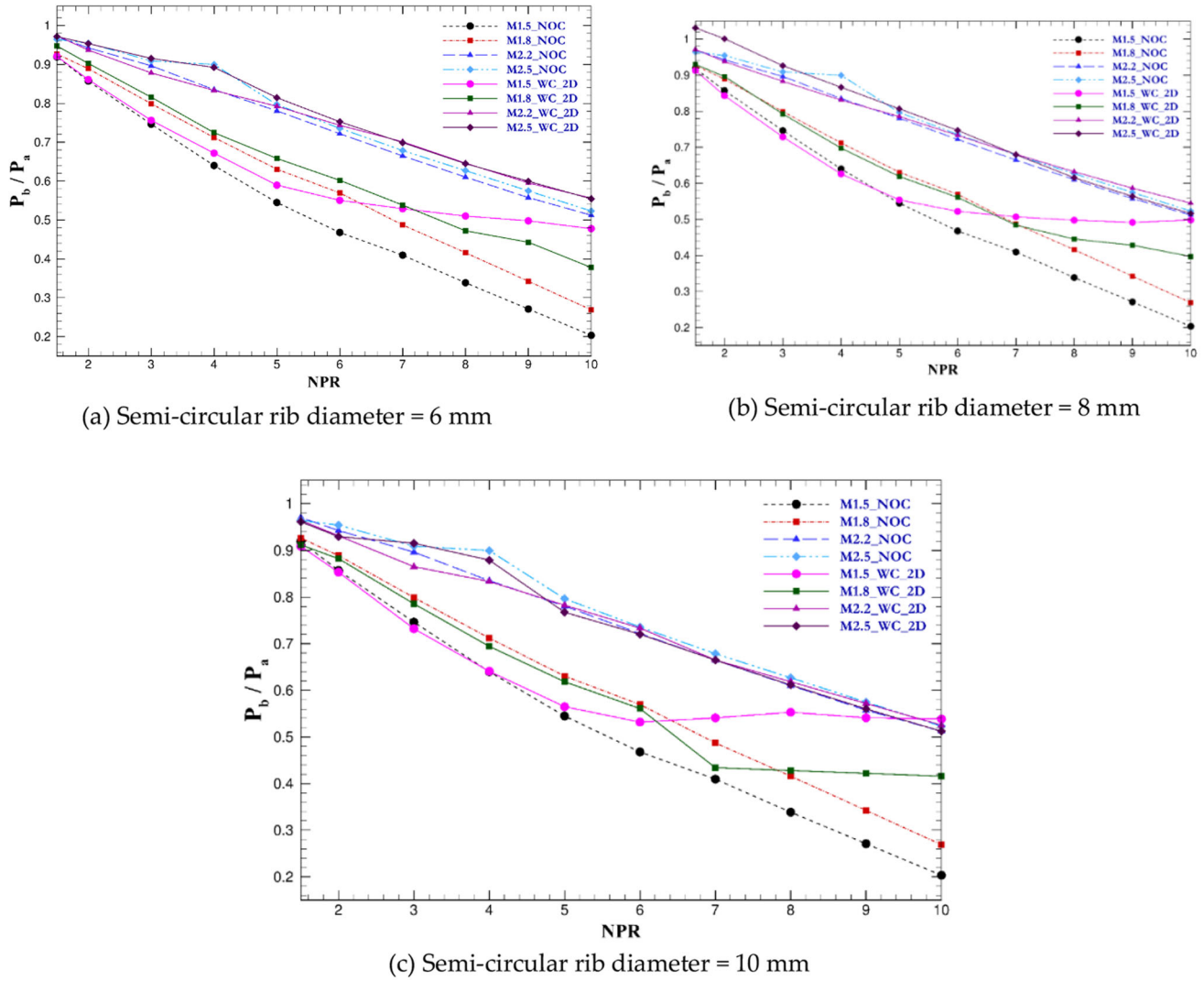


Fig. 8 Effect of semi-circular rib on base pressure at 2D and supersonic Mach number

2.2.1 Max error

The cumulative residual error is determined by max error, which captures the worst error between the expected and true values. In a perfectly fitted single-source regression model, a max error will be zero. This metric indicates the model's degree of error when the training is fitted, but this would not be probable in the real world. If \hat{a}_i is the value of the i th sample, and a_i is the true value, then the max error is defined as follows:

$$\text{Max Error } (a, \hat{a}) = \max(|a_i - \hat{a}_i|). \quad (1)$$

2.2.2 Mean absolute error

The MAE calculation function represents an absolute error, a risk measurement corresponding to the expected loss value. If the expected value of the i th sample is \hat{a} , and a_i is the appropriate true value and is defined as the absolute MAE, overestimate

$$\text{MAE } (a, \hat{a}) = \frac{1}{n_{\text{samples}}} \sum_{i=0}^{n_{\text{samples}}} |a_i - \hat{a}_i| \quad (2)$$

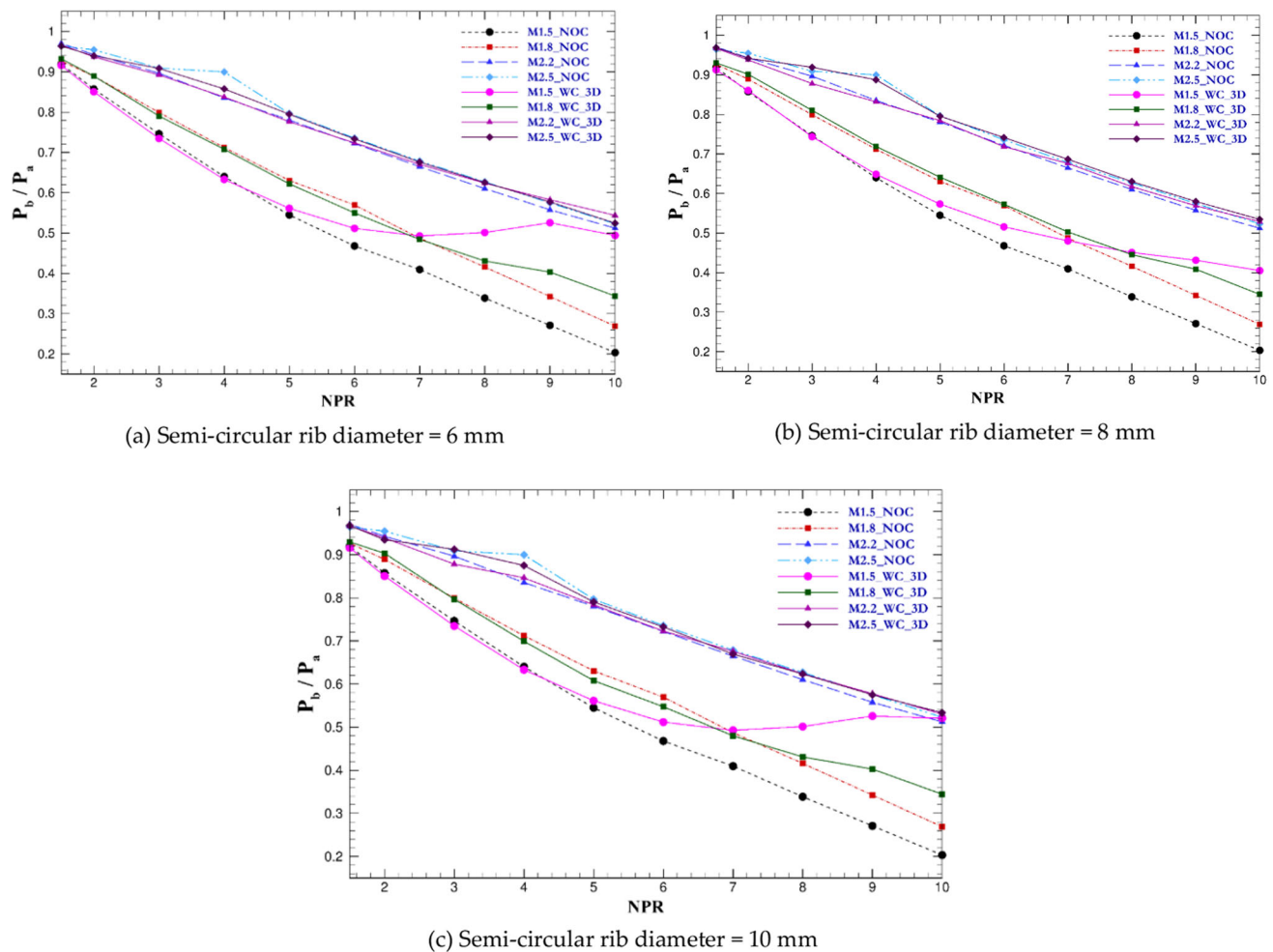


Fig. 9 Effect of semi-circular rib on base pressure at 4D and supersonic Mach number

2.2.3 Mean squared error

The MSE function calculates the mean square error, a risk metric corresponding to the squared (quadratic) error or loss value predicted. If \hat{a}_i is the expected sample value and a_i the corresponding true value, then the mean n sample squared error (MSE) is defined as

$$\text{MSE}(a, \hat{a}) = \frac{1}{n_{\text{samples}}} \sum_{i=0}^{n_{\text{samples}}-1} (a - \hat{a})^2 \quad (3)$$

2.2.4 Median absolute error

The MeAE is interesting because it is resilient to outliers. Given data, the loss (percent) is determined by taking the median of all absolute differences between the target and the estimate. If the \hat{a}_i value of the i th is estimated, and the a_i value is the true value of the i th value, then the n sample-MeAE is defined as follows:

$$\text{MedAE}(a, \hat{a}) = \text{median}(|a_1 - \hat{a}_1|, \dots, |a_n - \hat{a}_n|) \quad (4)$$

2.2.5 Mean Poisson, gamma, and Tweedie deviances (MTD)

The MTD function calculates the mean-deviance of the Tweedie by power parameter (P). This is a measure that generates expected regression target expectation values. There are exceptional circumstances equal to MSE if power = 0, mean Poisson deviance when

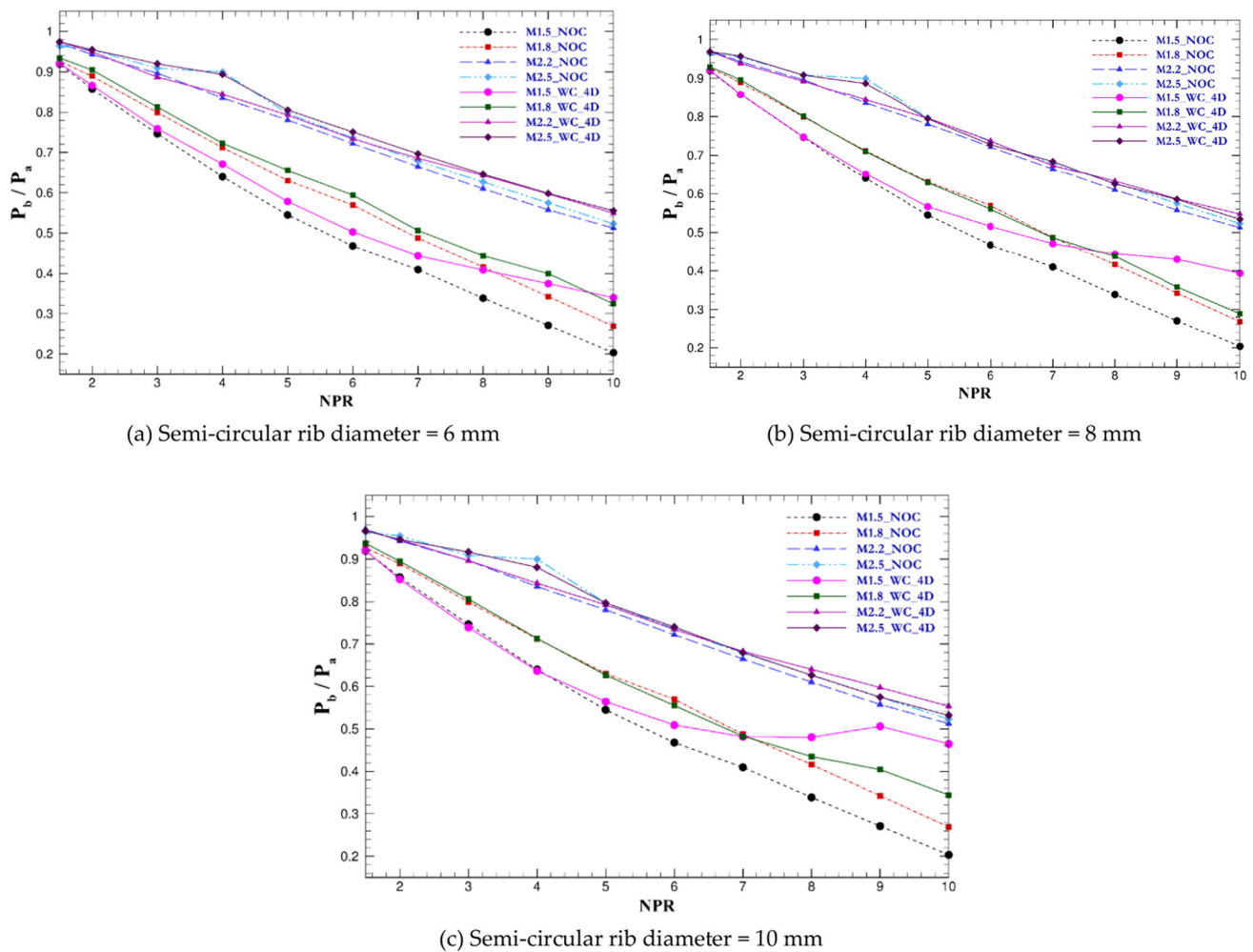


Fig. 10 Effect of semi-circular rib on base pressure at 3D and supersonic Mach number

power = 1, and mean gamma deviance when power = 2. If \hat{a}_i is the predicted sample value, and a_i is the appropriate true value, then the mean Tweedie deviance (D) error for power p is defined as estimated by n_{samples}

$$D(a, \hat{a}_i)^2 = \frac{1}{n_{\text{samples}}} \sum_{i=0}^{n_{\text{samples}}-1} \begin{cases} (a_i - \hat{a}_i)^2, & \text{for } p = 0(\text{Normal}) \\ 2(a_i \log(a_i/\hat{a}_i) + \hat{a}_i - a_i), & \text{for } p = 1(\text{Poisson}) \\ 2(\log \hat{a}_i/a_i) + a_i/\hat{a}_i - 1, & \text{for } p = 2(\text{Gamma}) \\ 2\left(\frac{(\max(a_i, 0)^{2-p})}{(1-p)(2-p)} - \frac{a\hat{a}_i^{1-p}}{1-p} + \frac{\hat{a}_i^{2-p}}{2-p}\right), & \text{Otherwise} \end{cases} \quad (5)$$

Tweedie variance is a degree two-power homogeneous function. Gamma distribution with power = 2 implies no effect on deviance by scaling y true and y pred. Deviance linearly scales for Poisson distribution power = 1 quadratically for normal distribution (power = 0). Extreme deviations between true and predicted targets are given higher power and less weight. For example, we compare the two predictions of 1.0 and 100, both of which are 50% of their true values. The mean square error (power = 0) is very sensitive to the second point prediction difference.

3 Discussion

This study aims to control the flow field of a suddenly expanded duct at sonic and supersonic Mach numbers. We identified the critical Mach numbers that dictate the base pressure while selecting the Mach numbers for the study. The measured parameters were the base pressure, wall pressure along the duct, and pressure loss. These variables were normalized with ambient pressure. The pressure loss was estimated by recording the stagnation pressure at the main settling chamber and the duct's exit plane using a pitot tube. The pressure deficit is determined to evaluate the pressure loss based on these two values. The analysis is carried out in two

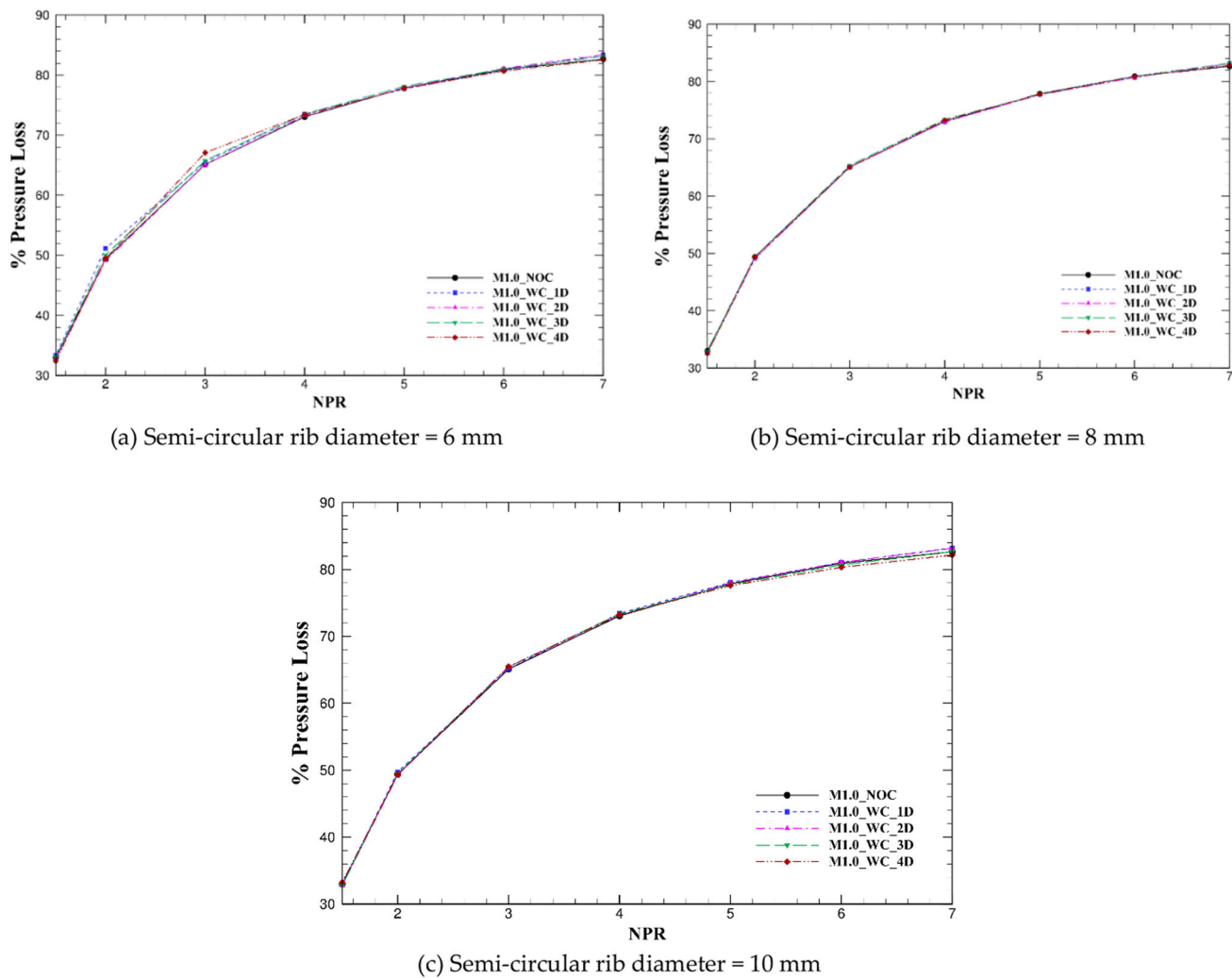


Fig. 11 Pressure loss at sonic Mach when rib diameter is equal to **a** 6 mm **b** 8 mm **c** 10 mm

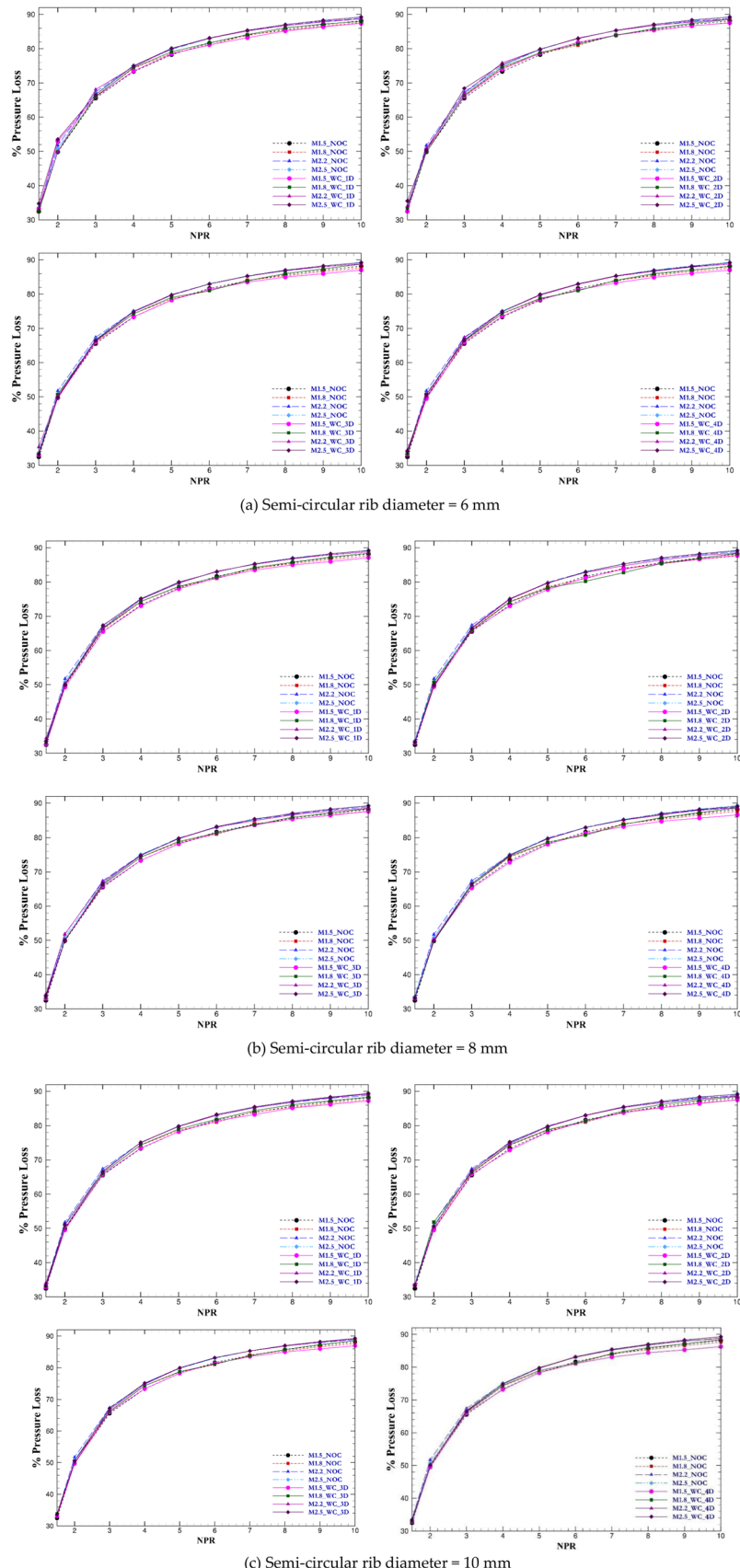
phases. The first phase/section performs the experimental study of base pressure, pressure loss, and wall pressure. A comparative analysis is made between flow with no control (NOC) and having control (WC). Passive control in semi-circular ribs is provided where the effect of rib diameter and its location from the base is assessed. Sonic and supersonic Mach nozzles with NPR in the range 3 to 11 are also investigated for pressure changes. In the second section, the pressure values are modeled, and the training and testing results are analyzed in detail using all the sixteen models developed.

3.1 Base pressure at sonic Mach number

The effect of the passive semi-circular rib of different diameters located at several positions on the duct is studied in this section. The diameters of the semi-circular rib chosen are 6, 8, and 10 mm. The rib positions are at 1D, 2D, 3D, and 4D away from the duct's base, where D is the duct's width. Figure 6 shows non-dimensional base pressure variation with NPR from 1.5 to 7 at the sonic Mach number. The flow from the nozzle becomes under-expanded from NPR 2 and above. The outcomes indicate that the base pressure follows the same pattern with no control (NOC) (i.e., no rib placed on the duct wall) and control (WC) (i.e., rib placed on the duct wall) when the rib diameter increases and the ribs' locations shift away from the base. However, the effect of having a rib on the duct wall at different locations is much more apparent compared with base pressure having no control.

The influence is not evident till NPR 4, after which the base pressure with passive control becomes significant. The oblique shocks are formed as a lower NPR, and an adverse pressure gradient causes this effect. The pressure gradient is favorable, and the flow over-expands for higher NPR. Although NPR 1.89 is required for a correctly expanded nozzle at sonic Mach, the ribs are helpful only for a much higher value. The duct's area ratio is 7.84 because the duct width is 28 mm, and the reattachment is comparatively large. Accordingly, the rib is ineffective in causing an increase in the base pressure even at lower NPR (<4). The physics may be

Fig. 12 Pressure loss at supersonic Mach numbers rib diameter is of 6 mm, 8 mm, and 10 mm



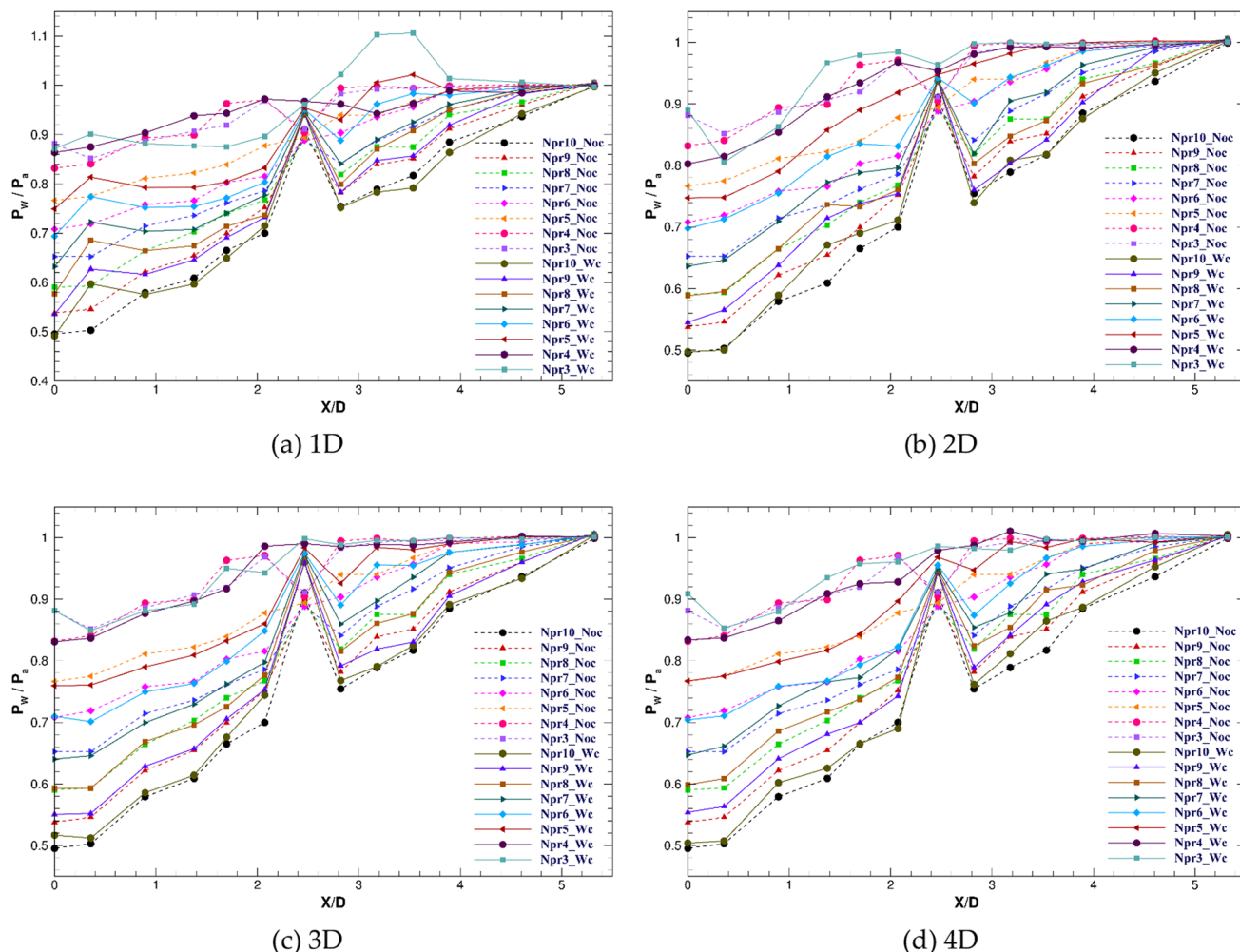


Fig. 13 At Mach 2.2, wall pressure variations having rib (6 mm) and no rib at different locations

when the relief effect from the rise of the area ratio is beyond a certain limit. The flow from the converging nozzle discharged into the enlarged duct tends to attach with reattachment length other than the optimum for a strong vortex at the base.

This process makes the NPR effect on base pressure insignificant for a higher area ratio. Otherwise, the decreasing trend in the base pressure must stop when the nozzles are under-expanded, and the base pressure should increase. This trend is seen in the literature for lower area ratios in the range of two to four. Next, the rib at location 4D is less effective than that at location 1D/2D after NPR 4. Flow reversal occurs due to rib presence because the reattachment of flow with the duct wall occurs between 2 and 3D. This flow reversal appears at the base, causing an increase in the base pressure. At 1D or 4D, the rib does not help in flow reversal, resulting in a minimal rise in the base pressure because they are before or away from the reattachment point. At lower NPRs, the passive control results in a decrease in the base pressure. This finding is in line with researchers' discovery, indicating that either active or passive control when the nozzles are over-expanded controls the base pressure area ratio greater than five. The same is observed for all rib diameter cases up to NPR 4, and passive control reduces the base pressure.

This trend is due to the combined effect of area ratio, NPR, Mach number, rib diameter, the interaction of the shock waves within and outside the reattachment area, and rib locations. The flow is greatly disturbed at the duct wall with the increase in the rib diameter from 6 to 8 mm, causing more fluid to reverse. This situation also causes an increase in the base pressure. At lower NPRs, the control results in a decrease in the base pressure because the nozzles are over-expanded. Ribs with 6 and 10 mm diameters located at 28 and 56 mm from the base are most effective. The effect is maximum at a 10 mm rib diameter. At this diameter, the rib's location is insignificant because the flow reattachment is affected by the rib's increasing diameter. Thus, an upper limiting value of the rib diameter exists at which the rib's location does not cause significant variations in the base pressure.

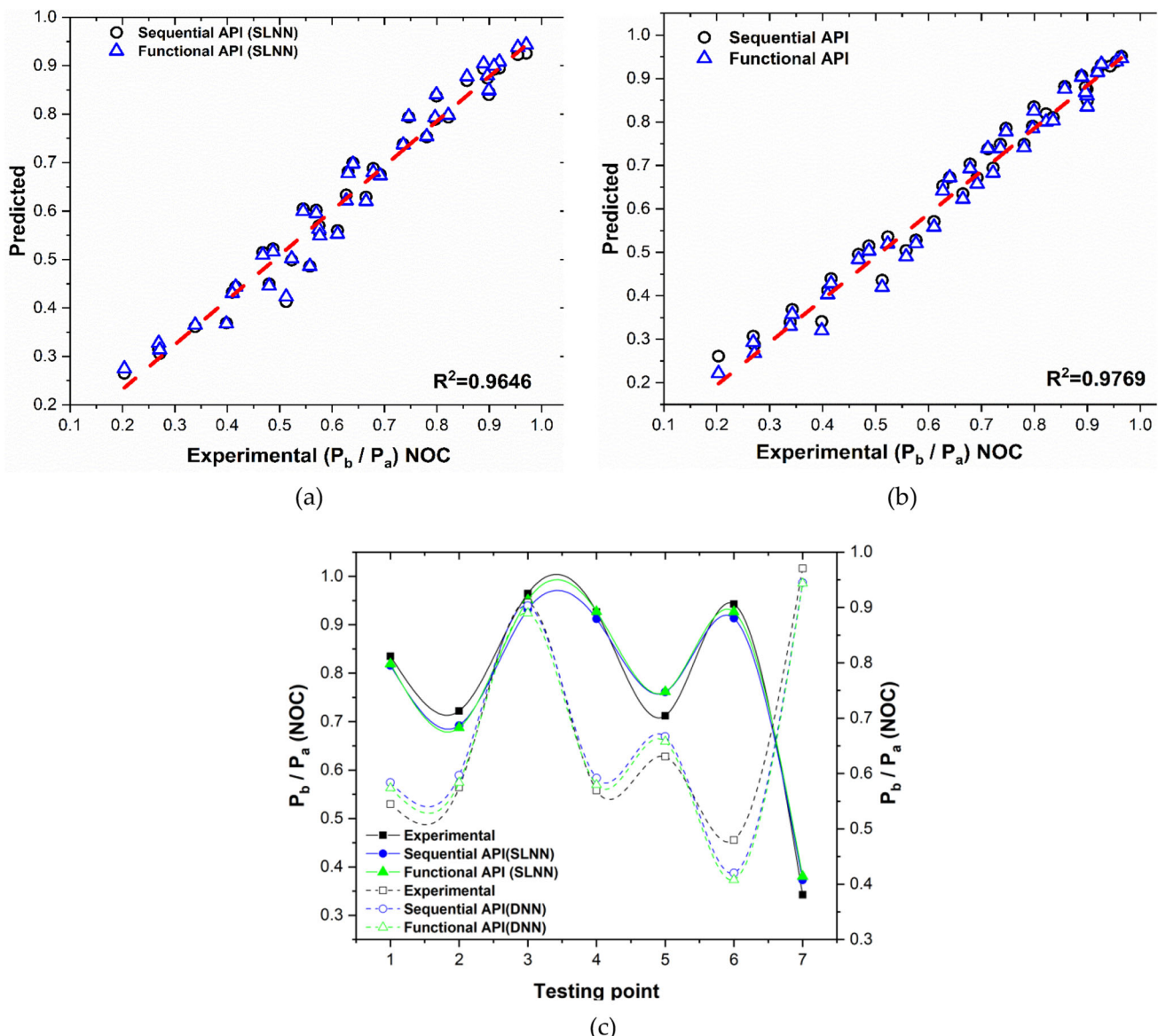


Fig. 14 Fitting/prediction of base pressure having NOC (no control) using **a** SLNN and **b** DNN adopting sequential and functional APIs for training and **c** testing

3.2 Base pressure at supersonic Mach number

The variations in the base pressure of the flow expanded from a square nozzle into the square duct are studied for four supersonic Mach numbers. The trend followed is in line with the sonic Mach number for increasing NPR, as shown in Fig. 7 at 1D rib position at the duct wall. The passive control effectiveness was visible after NPR 4 when the nozzle was operating at design NPR. In this case of Mach 1.5, 1.8, 2.2, and 2.5, the base pressure decreases with increased NPR. Adverse pressure gradient exists at the nozzle exit with oblique shock formation at Mach 2.2 and 2.5.

However, at lower Mach numbers, the decreasing trend in the base pressure continues despite the nozzle being under-expanded. This phenomenon may be due to the considerable reattachment length. The high duct width also reduces the base's suction even if it is increased for higher levels of over-expansion. The design NPRs for Mach 1.5, 1.8, 2.2, and 2.5 are 3.67, 5.74, 10.69, and 17.08, respectively. The base pressure continuously declines for the flow in the duct with no rib (NOC). The base pressure with rib at the 1D location is affected for Mach 1.5 and 1.8 because the design NPRs are within $NPR = 6$. After NPR 5, the base pressure rises for the lower Mach numbers 1.5 and 1.8 as the flow after NPR 4 and 5 are under-expanded.

Flow reversal occurs at the 1D location at rib diameters 6 and 8 mm, increasing the base pressure. The reattachment point for high Mach numbers 2.2 and 2.5 is farther than 2D because no effect of the rib is seen, and the correctly expanded flow occurs only after

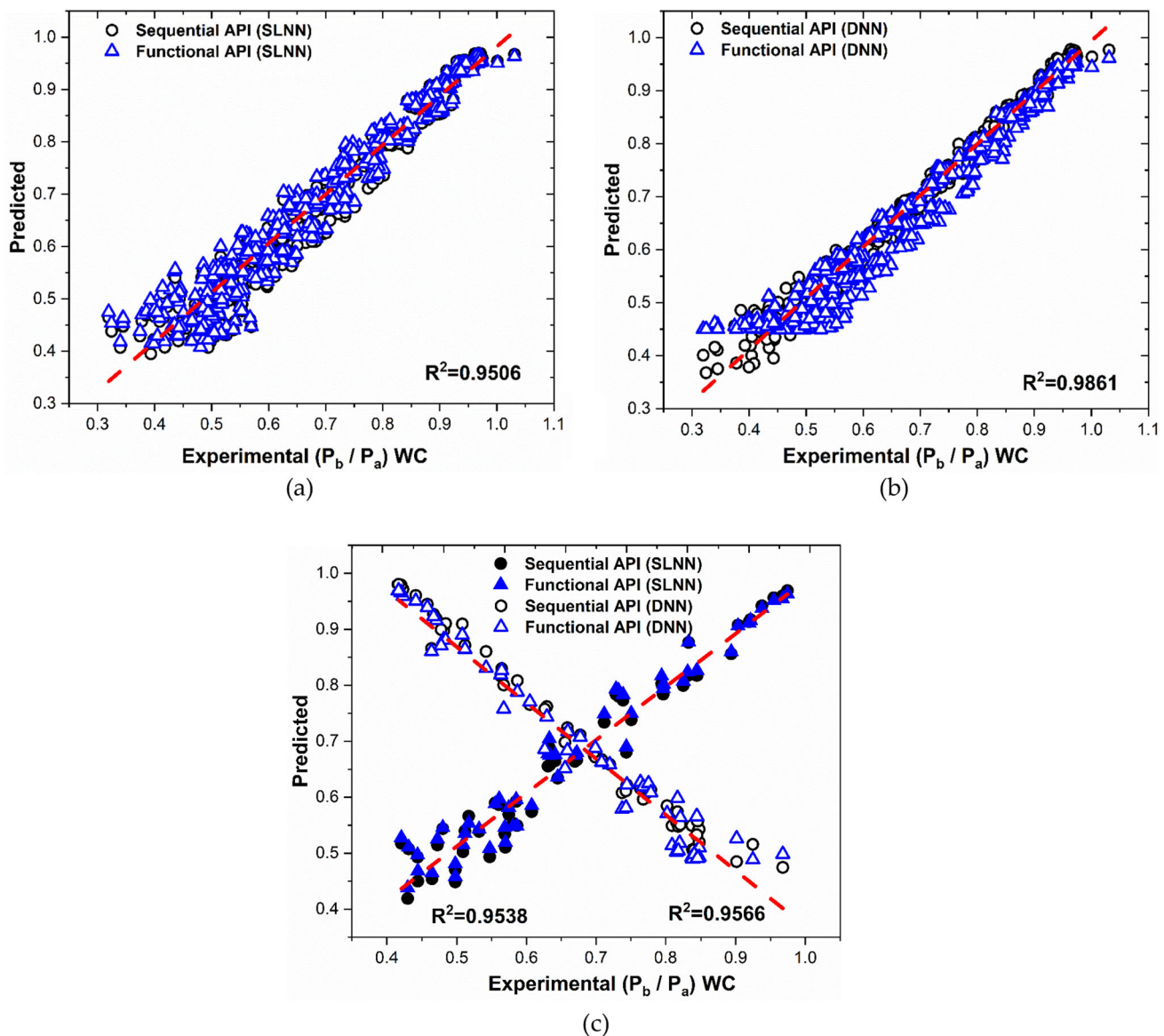


Fig. 15 Fitting/prediction of base pressure WC (having control) using **a** SLNN and **b** DNN adopting sequential and functional APIs for training and **c** testing

NPR 10 in these two Mach numbers. The impact on the base pressure is the same 8 to 10 mm rib diameter; the result is proficient. The reattachment of flow occurs due to increased rib diameter as the flow experiences its presence, causing more fluid entrapment at the base and increased base pressure. Figures 8, 9 and 10 show the base pressure variations when the semi-circular ribs of 6 to 10 mm are positioned at 2D, 3D, and 4D away from the duct's base, respectively.

The base pressure with NOC and with rib is shown for supersonic Mach numbers. The trend followed in this case is also like in the preceding discussion. The negligible effect of the rib at Mach 2.2 and 2.5 is confirmed in this case because the flow is purely over-expanded. At Mach 1.5 and 1.8, the rib effectiveness is seen after NPR 5 due to a favorable pressure gradient. If the NPR is increased beyond ten, then the under-expanded flow will undoubtedly influence the base pressure due to the rib. However, this NPR above ten cannot be achieved due to the experimental limitations. When the NPR is above five, the rib effectiveness significantly increases due to flow under-expansion and a favorable pressure gradient. In this case, the rib diameter of 10 mm is more effective than the 6 and 8 mm. When the rib is placed at 2D, it results in a considerable increase in the base pressure compared with the 1D rib location.

The flow reversal becomes slightly complicated when the rib is positioned at 3D because the primary vortex is far away, as shown in Fig. 9. Accordingly, the base pressure with the rib is not as significant as in the previous 2D case. The jet pump action of fluid entrapment and ejection into the mainstream is not helpful due to less mass reaching the base's dead zone. Nevertheless, the base pressure rise at Mach 1.5 is visible to a certain extent as the flow is correctly expanded at the lower NPR itself. In line

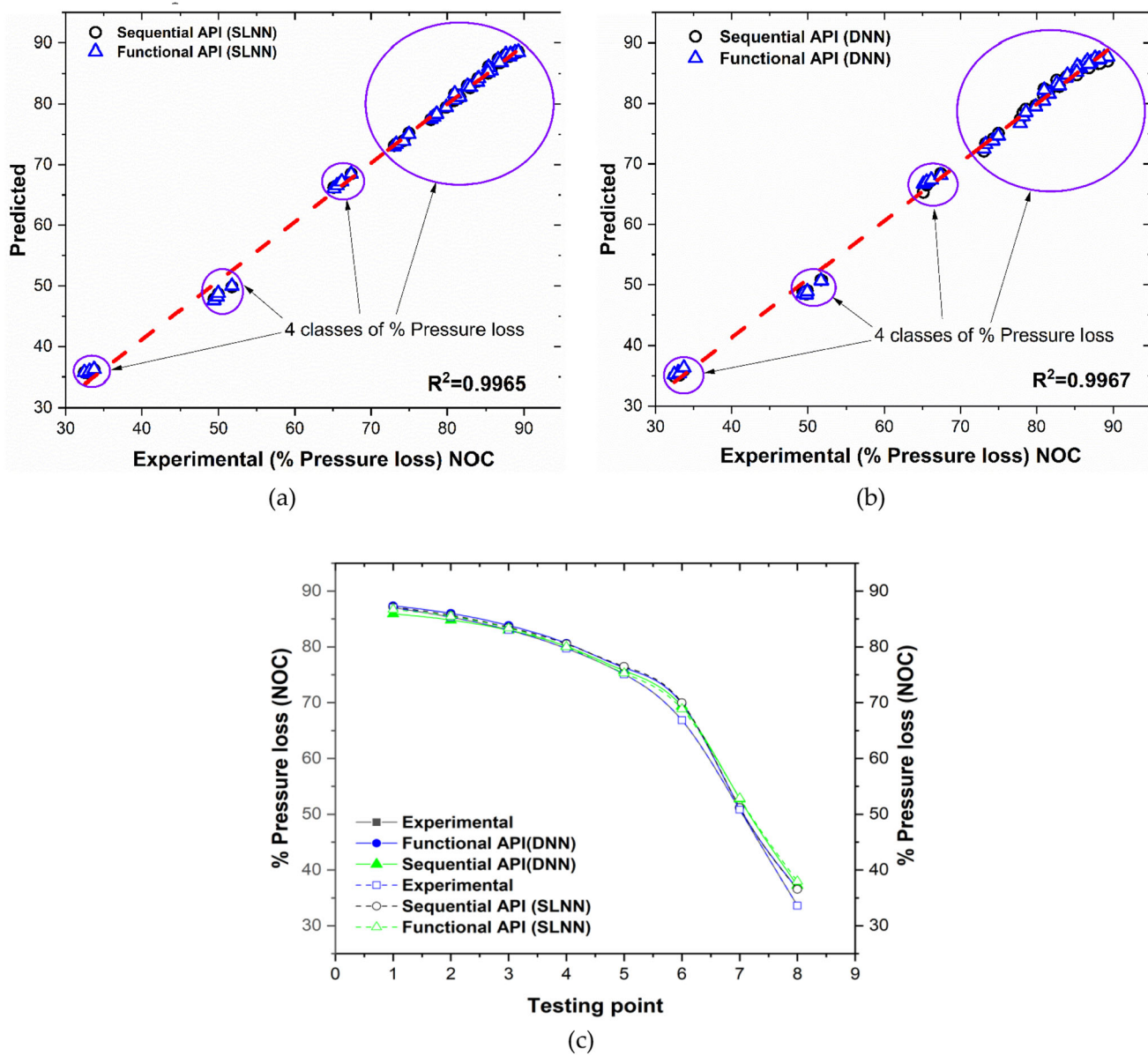


Fig. 16 Fitting/prediction of percentage pressure loss with NOC (no control) using **a** SLNN and **b** DNN adopting sequential and functional APIs for training and **c** testing

with the minimal effect of the rib with increasing location, the base pressure changes at 4D are obsolete for all NPR, as shown in Fig. 7. At Mach 1.5, a certain improvement is visible at a significantly higher level of under-expansion when the rib is 10 mm. This phenomenon is purely due to the striking of fluid to this large rib, even if it is far. The analysis shows that the base pressure variation is negligible if the rib is moved further at the 5D location, indicating lower and upper limiting values due to its diameter and location.

3.3 Pressure loss (NOC and WC)

Figure 11 shows the percentage pressure loss at sonic Mach number with NPR, rib location, and diameter. In this figure, the pressure loss remains the same irrespective of any given rib location or diameter. The pressure loss exponentially increases only with the increase in NPR. This notion is easily understood because increased input pressure and flow to achieve atmospheric pressure at the duct cause this exponential growth in pressure loss with NPR.

One thing to note is the lower gradient of pressure at higher NPR, which is evident as the flow is undergoing under-expansion with duct length remaining constant. If the duct length is reduced, then there may be chances of pressure loss significantly affected as the shocks and expansions are incomplete at a lower duct length. When the flow passes through the duct, the duct's surface friction and interactions of the shock waves play an essential role. The presence of the rib and its location has not shown any significant

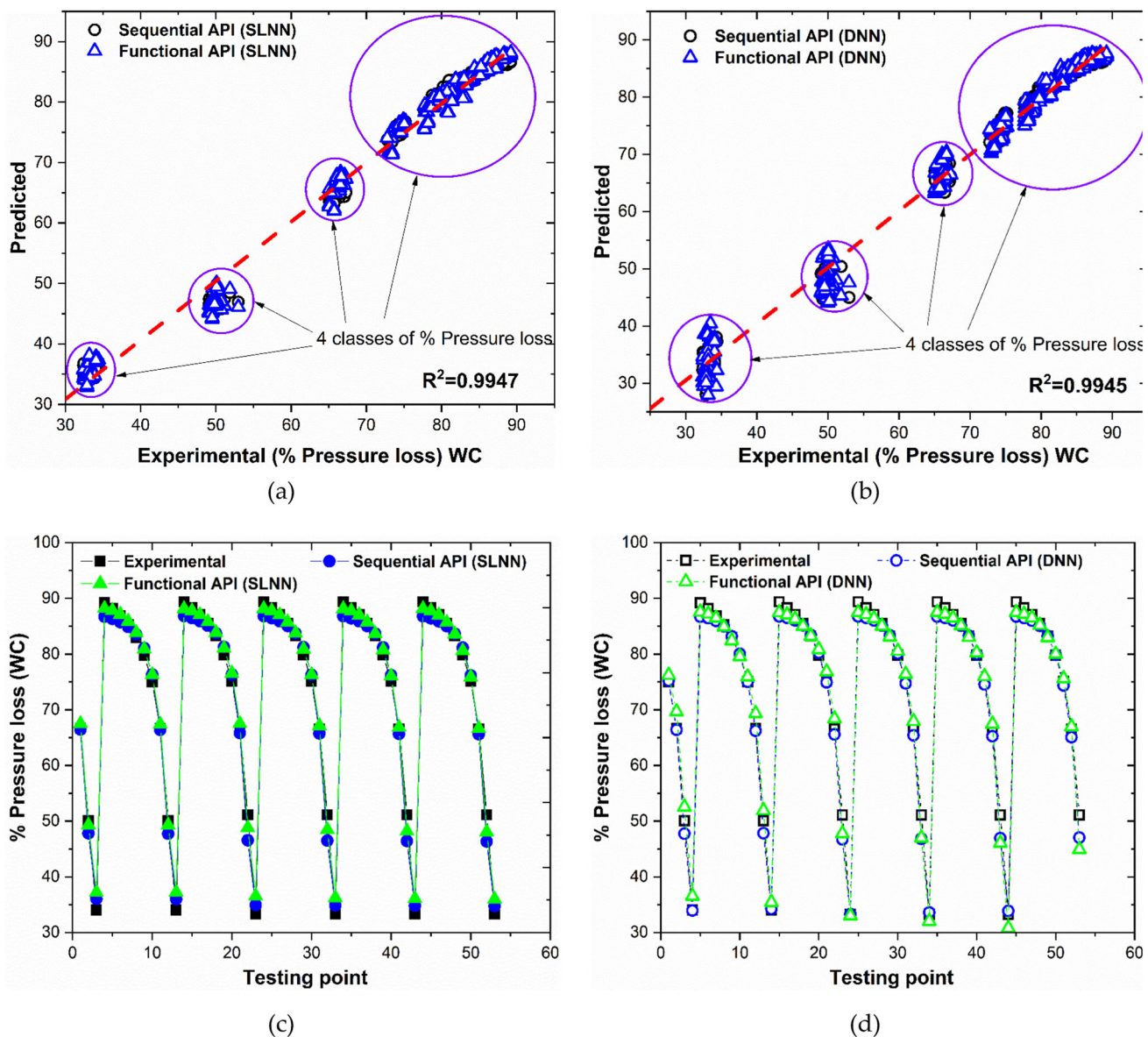


Fig. 17 Fitting/prediction of pressure loss WC (with control) using **a** SLNN and **b** DNN adopting sequential and functional APIs for training and **c** testing of SLNN **d** testing of DNN

increase in pressure loss. This notion indicates that using a passive control device in the semi-circular rib does not add extra losses, which is a positive sign of further usage in aerodynamic applications.

Figure 12 shows the pressure loss at supersonic Mach numbers with no control and rib at different locations, and the diameter is shown in detail. The pressure loss pattern is similar to what was seen at sonic Mach numbers. There is an overall increase in pressure loss at higher NPR at these supersonic Mach numbers. The pressure loss increases with an increase in NPR, which is purely a function of flow trying to reduce its pressure to reach the atmospheric pressure by forming shocks and expansion fans. Flow friction is another critical factor accounting for pressure loss. However, the introduction of ribs at different locations and sizes does not impact supersonic Mach numbers' pressure losses.

3.4 Wall pressure (NOC and WC)

Figure 13 shows the wall pressure variations with the increasing NPR and rib locations/diameter. The wall pressure is non-dimensionalized with D . The pressure tappings at the duct walls are placed to measure the effect of ribs on the wall pressure. Only a supersonic flow is adopted for the sake of brevity. The pattern remains the same for the remaining Mach numbers. Figure 10 shows that the presence and absence of the ribs do not significantly affect the wall pressure. Although some variations are apparent

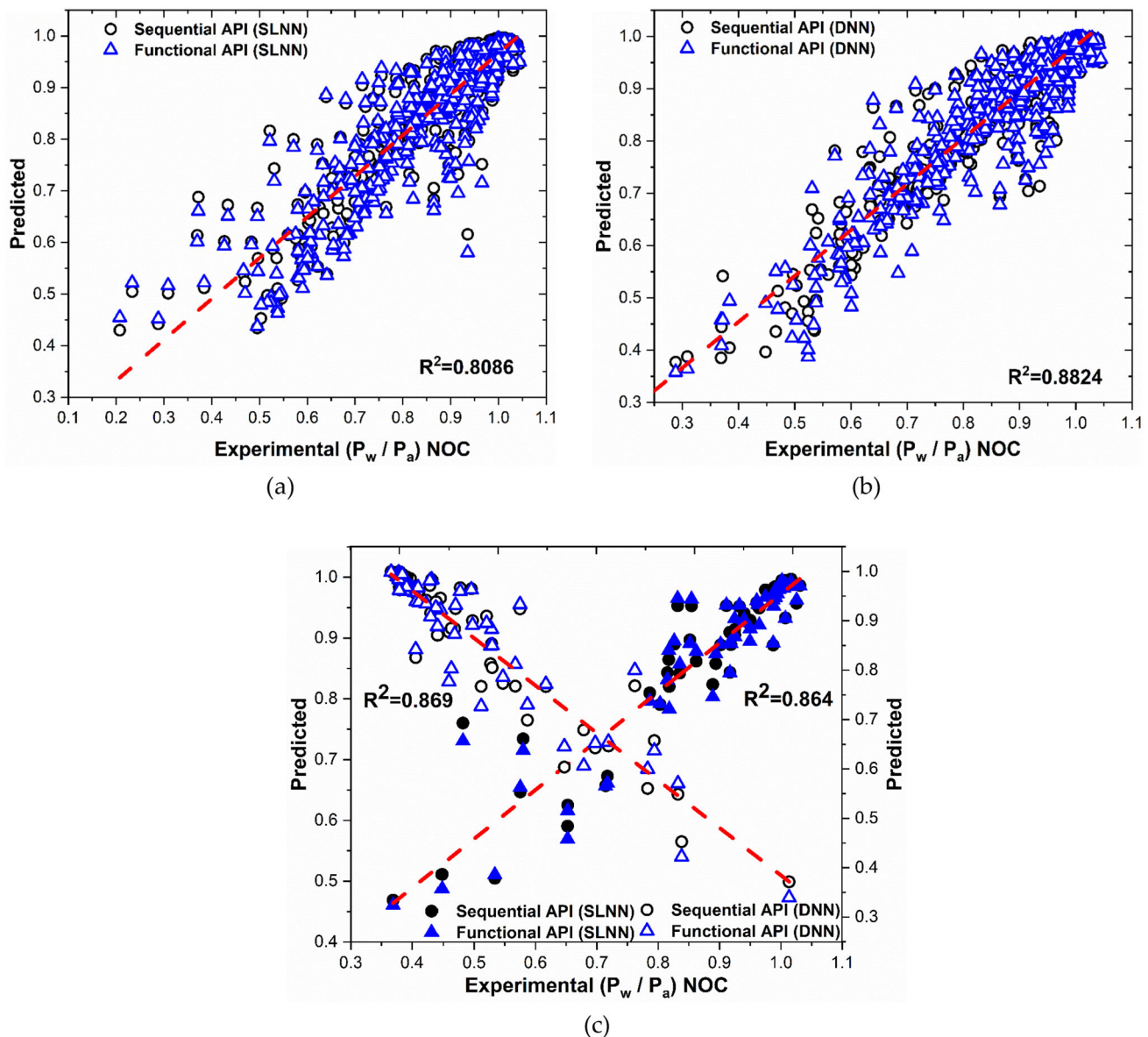


Fig. 18 Fitting/prediction of wall pressure with NOC (no control) using **a** SLNN and **b** DNN adopting sequential and functional APIs for training and **c** testing

as the flow field is affected with the rib at the wall, any significant wall pressure fluctuations are not observed, indicating that ribs are safe. An increase in wall pressure is observed with only a slight jump at a few locations.

At the duct exit, the atmospheric pressure is attained at all the NPRs, which is in agreement with the previous discussion of pressure loss. Some fluctuations in the pressure distribution in the duct can be observed. Such a phenomenon may be because when the flow expands, it collides with the duct wall and grows. This compression of flow and expansion causes a rise and drop of pressure along the duct wall, as observed from the wall pressure figures. The passive control does not aggravate the flow field in the duct, which is a critical outcome.

3.5 Modeling using SLNN and DNN

As previously mentioned, the flow at sonic and supersonic Mach numbers having no control (NOC) for the base pressure and percentage pressure loss is separately modeled due to the different input parameters involved in the flow with control (WC). The wall pressure involving another two new inputs is again separately modeled for the NOC and WC cases. The complete readings belonging to base pressure, pressure loss, and wall pressure are taken as a data set separately. A total of four models, namely, single-layered neural networks (SLNN) and DNNs using sequential API or functional API adopted for regression analysis, provide

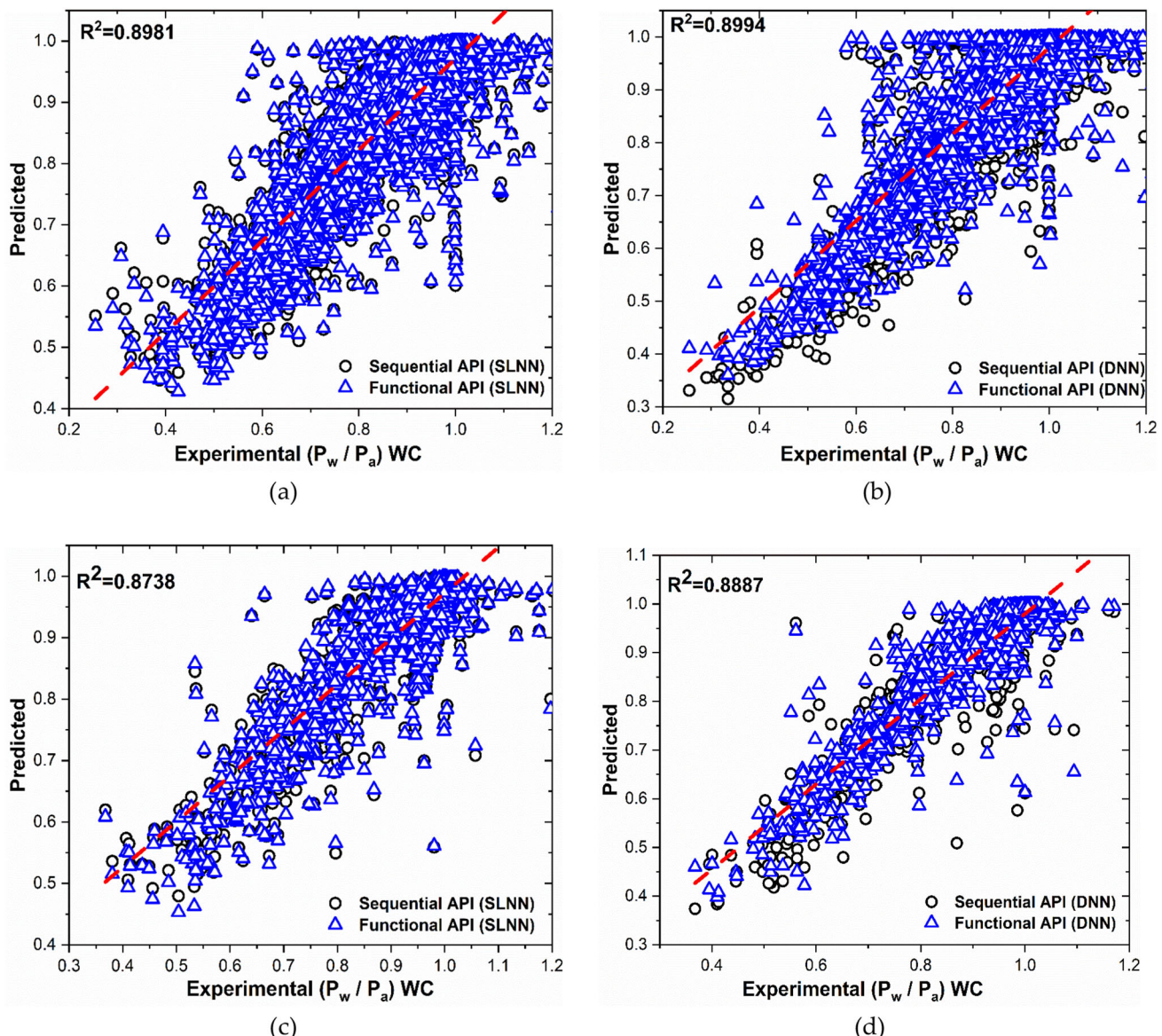


Fig. 19 Fitting/prediction of wall pressure WC (with control) using **a** SLNN and **b** DNN adopting sequential and functional APIs for training and **c** testing of SLNN **d** testing of DNN

a completely different set of results. Sequential and functional API results are combined in a single plot in case of training output to avoid the article's length. The testing results are separately plotted for the sake of clarity.

3.5.1 Base pressure with NOC

Figure 14a, b shows the fitted values of the base pressure at all Mach numbers and NPR with the experimentally measured output, as obtained by the sequential and functional APIs of the SLNN and DNN models. The R^2 (coefficient of determination) of the fitted value with the red trend is shown in both figures. The R^2 value of SLNN is 0.9646 compared with 0.9769 of DNN, indicating a better accuracy of the latter. The deep learning ability of the DNN model results in a proper mapping of weights and bias functions compared with a single-layered model, indicating better accuracy. The sequential and functional API models do not affect the ability much because they are almost overlapped. The testing results of the four models are depicted in Figure 14c. The testing results are in excellent agreement with the experimental and modeling output. Therefore, all the models are bucketful in predicting the base pressure with NOC.

The base pressure with Mach numbers, NPR, semi-circular rib diameter, and the rib's location as the input parameters for flow with passive control is modeled in the next phase. The modeling results using the SLNN and DNN algorithms' sequential and functional APIs are provided in Figure 15a, b of the training phase. The testing results are provided in Figure 15c of all the models

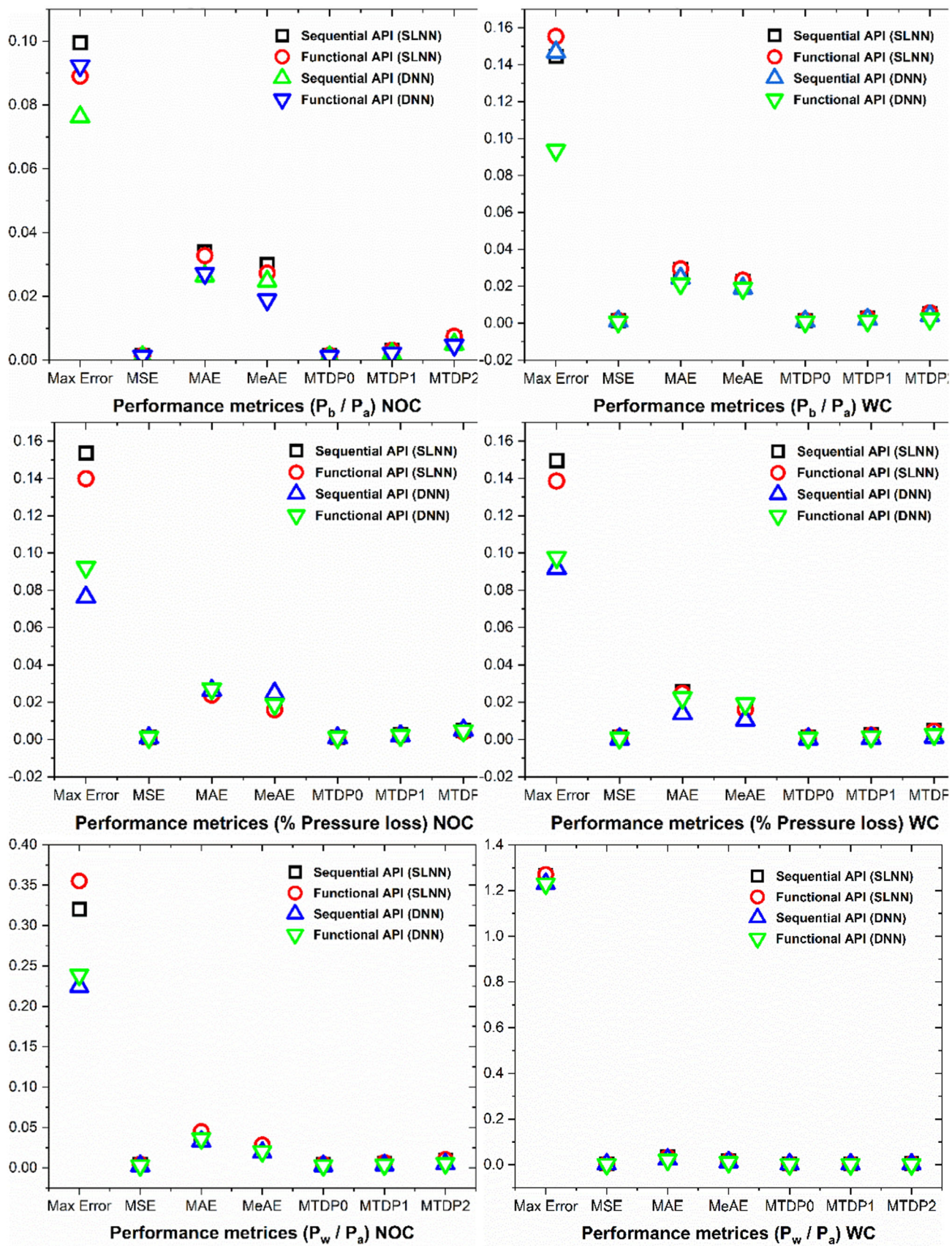


Fig. 20 Evaluation of performance metrics to assess the loss and accuracy of different models with different sets of data having NOC and WC

for base pressure WC. The figures show that the base pressure with four inputs entirely agrees with the SLNN and DNN models. The algorithms with both APIs show a good match with the experimental readings.

The more comprehensive model adopted in this study with 12 neurons in each layer can easily predict highly nonlinear data. The R^2 value of a single-layered network between the measured and the fitted values is 0.9506, whereas that of the deep networks is 0.9861. This result indicates that the deeply layered model is more capable than the single-layered one. The number of iterations for the SLNN model was maintained at 500, while only 200 iterations were adopted for DNN to obtain better accuracy. This notion implies that the DNN model's ability to obtain the predictions is reasonably quick.

The testing results in Figure 15c show the algorithm's importance and accuracy. The SLNN and DNN values for the experimental readings are plotted. The readings from DNN are close to the trendline than those from the SLNN model. The readings from DNN are more compact than those from the SLNN model; hence, DNN is most suitable for predicting base pressure with or without control. However, the SLNN model predictions are also with reasonable accuracy, which cannot be neglected. These models' abilities will be explored for more highly nonlinear wall pressure data in the upcoming sections.

Figure 16a, b shows the SLNN and DNN model predictions for percentage pressure loss. The pressure loss values for flow having no control are modeled here. The percentage pressure loss using both the algorithms has the same accuracy because the data are not as highly nonlinear as base or wall pressure—a total of four groups of data points clustered due to regression. The higher pressure loss indicates the higher NPR values, while the lower class of pressure loss denotes a lower NPR.

The testing is also successful using both models because the experimental readings correlate, as shown in Figure 16c. The pressure loss obtained in flow WC is shown in Figure 17. The trained network providing the predictions during the supervised learning having known target values is shown in Figure 17a, b. The classes obtained are the same, and the accuracy provided by each model adopted in training/testing is in close agreement, hence a successful training and testing.

The wall pressure variations without passive control having Mach, NPR, and duct location as inputs are modelled using the proposed algorithms. The training results obtained as part of the fitted values for supervised learning of the model are shown in Figure 18a, b. The results indicate the dominating accuracy of the DNN model compared with SLNN. The predicted values using DNN are closer and compact, while the SLNN model predictions are slightly dispersed. The R^2 value for the wall pressure having NOC obtained from the SLNN model is far less than that acquired using DNN. This finding shows the ability of the DNN model to easily predict even highly nonlinear data. The comparison of the testing results compared with the experimental results shows that the R^2 value of the DNN model is better than that of the SLNN model.

Figure 19a, b shows the sequential and functional APIs' experimental and predicted values. Given the data set of wall pressure with a combination of five inputs, it has the highest number of readings compared with other characters. The dense plot of the combined sequential and functional APIs from a single model verifies the previous statement. The R^2 value obtained for control is more compared with the wall pressure modeling having no control.

The accuracy of both APIs increased compared with those in Figure 15 due to increased data. Both APIs have shown some differences where the DNN model performed better, as they did previously for base pressure and percentage pressure loss. In this case, the SLNN and DNN networks provide excellent agreement and accuracy for wall pressure, which is highly nonlinear, as previously depicted in Section 3.4. Approximately 15% of the total wall pressure data are randomly chosen by the algorithm using the sklearn library for testing. The testing results depicted in Figure 16c shows that the models and APIs appropriately predicted the wall pressure WC. Hence, the models can be used for the modeling and prediction of higher parameters.

Figure 20 shows the performance of the sequential and functional APIs used for SLNN and DNN modeling. The standard performance metrics used are maximum error (Max Error), MSE, MAE, mean Tweedie deviance with power 0, 1, and 2 represented as MTDP0, MTDP1, and MTDP2. The metrics above are analyzed for base pressure having NOC and WC, percentage pressure loss having NOC and WC, and wall pressure having NOC and WC.

The figures show that the Max Error is highest for SLNN APIs, while the DNN model has the least error. The APIs in the DNN model have shown the lowest error. This Max Error is the error between the predicted and the measured values. Hence, the max error is the lowest in the passive control due to more input combinations, giving a more extensive dataset. In the case of wall pressure, the error has converged, indicating that all models are nearly identical. The values for the remaining metrics are overlapped with the lowest loss involved in DNN modeling.

4 Conclusions

An experimental investigation is performed to improvise the base pressure for compressible flows that can cause a decrease in base drag in aerodynamic vehicles. Semi-circular ribs as passive control devices are used in the duct where the high-speed flow expands. Flow at sonic and supersonic Mach numbers with different levels of expansions are analyzed. Later, the enormous data semi-automatically generated is carried out for DNN modeling. The following conclusions are made pertinent to passive control and regression modeling of the flow pressures:

1. Base pressure at sonic Mach number declines even though a favorable pressure gradient exists without passive control. When the ribs are positioned at different locations, there is an increase in the base pressure for an NPR of more than four. The control

- results in a decrease in base pressure as the nozzles are over-expanded for lower NPRs. Ribs with 6 and 10 mm diameters located at 28 and 56 mm from the base are most effective.
2. The base pressure at higher NPR is significantly increased with rib for Mach 1.5 and 1.8. Further increasing the diameter of the rib helps in improving the base pressure. There is an upper limit to the rib location, after which the base pressure does not improve. At Mach 2.2 and 2.5, the base pressure continues to decrease even at the highest NPR, and passive control in the form of ribs decreases the base pressure as nozzles are over-expanded for the entire range NPR.
 3. The pressure loss ranges from 30 to 80% at sonic and 30% to 90% at sonic and supersonic Mach numbers. The location of ribs does not influence pressure loss significantly.
 4. The data generated has different vectors due to their attributes as base pressure and percentage pressure loss are combined, and wall pressure is separated. The flow WC adds two more inputs than without control; hence, it is separately modeled. This situation results in the formation of four NN models.
 5. The sequential and functional API models in SLNNs and DNNs do not inaccurately differ. However, the functional API is rarely observed to provide a slightly improved accuracy over sequential API.
 6. The DNN has provided good accuracy than the SLNN because of its training ability. The accuracy provided is suitable for a lower number of iterations than the single-layered network.
 7. Both algorithms provide nearly the same loss and accuracy metrics for wall pressure with massive data because the training is more supervised than in the case of base pressure and percentage pressure loss. The performance metrics also indicate that the DNN model provides lower error than the other model.
 8. The NN models can predict this highly sensitive data with acceptable accuracy and can be used for future analysis of aerodynamic flow data.

Author contributions AK: Conceptualization, Investigation, Data Curation, Writing—Original Draft Preparation; PR: Supervision, Funding Acquisition, Writing—Review and Editing; SSSJunior: Writing—Review and Editing.

Funding Open access funding provided by University of Pretoria. This research was funded by Universiti Sains Malaysia Grant No. 1001/P/AERO/8014120, and the APC was funded by Universiti Sains Malaysia.

Data availability statement The datasets generated during and/or analyzed during the current study are available from the corresponding author on reasonable request.

Declarations

Conflict of interest The authors declare that they have no known competing financial interests or personal relationships that could influence the work reported in this paper.

Open Access This article is licensed under a Creative Commons Attribution 4.0 International License, which permits use, sharing, adaptation, distribution and reproduction in any medium or format, as long as you give appropriate credit to the original author(s) and the source, provide a link to the Creative Commons licence, and indicate if changes were made. The images or other third party material in this article are included in the article's Creative Commons licence, unless indicated otherwise in a credit line to the material. If material is not included in the article's Creative Commons licence and your intended use is not permitted by statutory regulation or exceeds the permitted use, you will need to obtain permission directly from the copyright holder. To view a copy of this licence, visit <http://creativecommons.org/licenses/by/4.0/>.

References

1. A. Khan, P. Rajendran, J.S.S. Sidhu, Passive control of base pressure: a review. *Appl. Sci.* **11**(3), 1334 (2021)
2. J. Zhou, C.H. Sun, B. Daichin, Drag reduction and flow structures of wingtip sails in ground effect. *J. Hydrodyn.* **32**(1), 93–106 (2020)
3. H. Yousif Al-Daraje, N.N. Alderoubi, Effect of combination yaw angle variation and base bleeding for tractor-trailer drag reduction through experimental investigation and CFD. *J. Phys. Conf. Ser.* **1519**, 012017 (2020). <https://doi.org/10.1088/1742-6596/1519/1/012017>
4. V. Pesce, S. Silvestrini, M. Lavagna, Radial basis function neural network aided adaptive extended Kalman filter for spacecraft relative navigation. *Aerosp. Sci. Technol.* (2020). <https://doi.org/10.1016/j.ast.2019.105527>
5. S. Li, L. Li, W. Huang, Y. Zhao, J. Chen, Design and investigation of equal cone-variable Mach number waverider in hypersonic flow. *Aerosp. Sci. Technol.* (2020). <https://doi.org/10.1016/j.ast.2019.105540>
6. S. Gao, J. Liu, Adaptive neural network vibration control of a flexible aircraft wing system with input signal quantization. *Aerosp. Sci. Technol.* (2020). <https://doi.org/10.1016/j.ast.2019.105593>
7. J. Lu, J. Huang, F. Lu, Kernel extreme learning machine with iterative picking scheme for failure diagnosis of a turbofan engine. *Aerosp. Sci. Technol.* (2020). <https://doi.org/10.1016/j.ast.2019.105539>
8. C. Yan, Z. Yin, X. Shen, D. Mi, F. Guo, D. Long, Surrogate-based optimization with improved support vector regression for non-circular vent hole on aero-engine turbine disk. *Aerosp. Sci. Technol.* (2020). <https://doi.org/10.1016/j.ast.2019.105332>
9. K.M. Pandey, E. Rathakrishnan, Influence of cavities on flow development in sudden expansion. *Int. J. Turbo Jet Engines* **23**(2), 97 (2006)
10. E. Rathakrishnan, O.V. Ramanaraju, K. Padmanaban, Influence of cavities on suddenly expanded flow field. *Mech. Res. Commun.* **16**(3), 139–146 (1989)
11. P.R. Viswanath, S.R. Patil, Effectiveness of passive devices for axisymmetric base drag reduction at Mach 2. *J. Spacecr. Rockets* **27**(3), 234–237 (1990)

12. P.R. Viswanath, Passive devices for axisymmetric base drag reduction at transonic speeds. *J. Aircr.* **25**(3), 258–262 (1988)
13. P.R. Viswanath, Flow management techniques for base and afterbody drag reduction. *Prog. Aerosp. Sci.* **32**(2–3), 79–129 (1996)
14. K.M. Pandey, E. Rathakrishnan, Annular cavities for base flow control. *Int. J. Turbo Jet Engines* **23**(2), 113–128 (2006)
15. K.A. Pathan, P. Dabeer, S.A. Khan, Effect of nozzle pressure ratio and control jets location to control base pressure in suddenly expanded flows. *J. Appl. Fluid Mech.* **12**(4), 1127–1135 (2019). <https://doi.org/10.29252/jafm.12.04.29495>
16. N.S. Vikramaditya, M. Vijji, S.B. Verma, N. Ali, D.N. Thakur, Base pressure fluctuations on typical missile configuration in presence of base cavity. *J. Spacecr. Rockets* **55**(2), 335–345 (2018). <https://doi.org/10.2514/1.A33926>
17. P. Rajendran, V. Sethuraman, S.A. Khan, A cost-effective data acquisition instrumentation for measurement of base pressure and wall pressure in suddenly expanded flow-through ducts. *J. Adv. Res. Fluid Mech. Therm. Sci.* **60**(1), 112–123 (2019)
18. A. Khan, P. Rajendran, J.S.S. Sidhu, Passive control of base pressure: a review. *Appl. Sci.* **11**, 1334 (2021)
19. V. Sethuraman, P. Rajendran, S.A. Khan, Base and wall pressure control using cavities and ribs in suddenly expanded flows—an overview. *J. Adv. Res. Fluid Mech. Therm. Sci.* **66**, 120–134 (2020)
20. E. Rathakrishnan, Effect of ribs on suddenly expanded flows. *AIAA J.* **39**(7), 1402–1404 (2001)
21. K. Vijayaraja, S. Elongovan, E. Rathakrishnan, Effect of rib on suddenly expanded supersonic flow. *Int. Rev. Aerosp. Eng.* 196–199 (2008)
22. K. Vijayaraja, C. Senthilkumar, S. Elangovan, E. Rathakrishnan, Base pressure control with annular ribs. *Int. J. Turbo Jet Engines* **31**(2), 111–118 (2014). <https://doi.org/10.1515/ijtj-2013-0037>
23. S.A. Khan, M. Asadullah, J. Sadhiq, Passive control of base drag employing dimple in subsonic suddenly expanded flow. *Int. J. Mech. Mechatron. Eng.* **18**(3), 69–74 (2018)
24. S.A. Khan, M. Asdullah, F. A. G. M. A. Jalaluddeen, A.A. Ahmed, M. Baig, Passive control of base drag in compressible subsonic flow using multiple cavity. *Int. J. Mech. Prod. Eng. Res. Dev.* **8**(4), 39–44 (2018). <https://doi.org/10.24247/ijmpedaug20185>
25. M. Asadullah, S.A. Khan, M.E.M. Soudagar, T. R. Vaishak, A comparison of the effect of single and multiple cavities on base flows, in *2018 IEEE 5th International Conference on Engineering Technologies and Applied Sciences (ICETAS)* (2018), pp. 1–6
26. J. Kidd, An investigation of drag reduction using stepped afterbodies, in *27th Aerospace Sciences Meeting* (1989), p. 333
27. P.R. Viswanath, Drag reduction of afterbodies by controlled separated flows. *AIAA J.* **39**(1), 73–78 (2001)
28. A. Ibrahim, A. Filippone, Effect of streamwise slots on the drag of a transonic projectile. *J. Aircr.* **44**(6), 1865–1876 (2007)
29. A. Ibrahim, A. Filippone, Supersonic aerodynamics of a projectile with slot cavities. *Aeronaut. J.* **114**(1151), 15–24 (2010)
30. A.S. Platou, Improved projectile boat-tail. *J. Spacecr. Rockets* **12**(12), 727–732 (1975)
31. S.-M. Liang, J.-K. Fu, Passive control method for drag reduction for transonic projectiles, in *9th Applied Aerodynamics Conference* (1991), p. 3213
32. A. Agnone, V. Zakkay, W. Sturek, Effects of Boattail geometry on the aerodynamics of hypersonic projectiles, in *20th Aerospace Sciences Meeting* (1982), p. 172
33. A.M. Agnone, B. Prakasam, Hypersonic aerodynamics of non-axisymmetric boattailed bodies. *J. Spacecr. Rockets* **24**(2), 181–182 (1987)
34. E. Elawwad, A. Ibrahim, A. Elshabkaa, A.R.-D. Technology, U. 2020, Flow computations past a triangular boattailed projectile. *Def. Technol.* **16**(3), 712–719 (2020). Accessed Oct 17, 2020. Online Available: <https://www.sciencedirect.com/science/article/pii/S2214914719304465>
35. Y. Yang, H. Xu, J. Wang, G. Zha, Large-eddy simulation of base drag reduction with jet boat-tail passive flow control. *Procedia Eng.* **126**, 150–157 (2015)
36. S.A. Khan, E. Rathakrishnan, Active control of suddenly expanded flows from under expanded nozzles-Part II. *Int. J. Turbo Jet Engines* **22**(3), 163–184 (2005)
37. S.A. Khan, E. Rathakrishnan, Active control of suddenly expanded flows from underexpanded nozzles. *Int. J. Turbo Jet Engines* **21**, 233–254 (2004)
38. G.M. Fharukh Ahmed, M.A. Ullah, S.A. Khan, Experimental study of suddenly expanded flow from correctly expanded nozzles. *ARPN J. Eng. Appl. Sci.* **11**(16), 10041–10047 (2016)
39. J.D. Quadros, S.A. Khan, A.J. Antony, Investigation of effect of process parameters on suddenly expanded flows through an axi-symmetric nozzle for different Mach Numbers using design of experiments. *IOP Conf. Ser. Mater. Sci. Eng.* **184**(1), 1–8 (2017)
40. K.M. Pandey, V. Kumar, CFD analysis of four jet flow at Mach 174 with fluent software. *Int. J. Chem. Eng. Appl.* **1**(4), 302 (2010)
41. S.A. Khan, A. Aabid, C.A. Saleel, Influence of micro-jets on the flow development in the enlarged duct at supersonic Mach number. *Int. J. Mech. Mechatron. Eng.* **19**(01), 70–82 (2019)
42. V. Sethuraman, S.A. Khan, Base pressure control using micro-jets in supersonic flow regimes. *Int. J. Aviat. Aeronaut. Aerosp.* **5**(1), 1 (2018)
43. S.M.A. Kumar, E. Rathakrishnan, Characteristics of controlled Mach 2 elliptic jet. *J. Propuls. Power* **32**(1), 121–133 (2016)
44. A. Bajpai, E. Rathakrishnan, Control of a supersonic elliptical jet. *Aeronaut. J.* **122**(1247), 131–147 (2018)
45. R. Pinto, A. Afzal, L. D'Souza, Z. Ansari, A.D. Mohammed Samee, Computational fluid dynamics in turbomachinery: a review of state of the art. *Arch. Comput. Methods Eng.* **24**, 467–479 (2017). <https://doi.org/10.1007/s11831-017-9183>
46. A. Afzal, Z. Ansari, A. Faizabadi, M. Ramis, Parallelization strategies for computational fluid dynamics software: state of the art review. *Arch. Comput. Methods Eng.* **24**, 337–363 (2017). <https://doi.org/10.1007/s11831-016-9165-4>
47. A. Afzal, A. Aabid, A. Khan, S. Afghan, U. Rajak, T. Nath, R. Kumar, Response surface analysis, clustering, and random forest regression of pressure in suddenly expanded high-speed aerodynamic flows. *Aerosp. Sci. Technol.* **107**, 106318 (2020). <https://doi.org/10.1016/j.ast.2020.106318>
48. A. Afzal, I. Nawfal, I.M. Mahbubul, S.S. Kumbar, An overview on the effect of ultrasonication duration on different properties of nanofluids. *J. Therm. Anal. Calorim.* **135**, 393–418 (2019). <https://doi.org/10.1007/s10973-018-7144-8>
49. A. Afzal, M. Abdul Mujeebu, Thermo-mechanical and structural performances of automobile disc brakes: a review of numerical and experimental studies. *Arch. Comput. Methods Eng.* **26**, 1489–1513 (2019). <https://doi.org/10.1007/s11831-018-9279-y>
50. R. Jilte, A. Afzal, S.A. Panchal, Novel battery thermal management system using nano-enhanced phase change materials. *Energy* **219**, 119564 (2021). <https://doi.org/10.1016/j.energy.2020.119564>
51. A. Asif, S.A. Khan, C.A. Salee, Role of ultrasonication duration and surfactant on characteristics of ZnO and CuO nanofluids. *Mater. Res. Express* **6**, 1150d8 (2019). <https://doi.org/10.1088/2053-1591/ab5013>
52. L. Samyilingam, N. Aslfattahi, R. Saidur, S. Mohd, A. Afzal, Solar energy materials and solar cells thermal and energy performance improvement of hybrid PV/T system by using olein palm oil with MXene as a new class of heat transfer fluid. *Sol. Energy Mater. Sol. Cells* **218**, 110754 (2020). <https://doi.org/10.1016/j.solmat.2020.110754>
53. A. Afzal, S. Alshahrani, A. Alrobaian, A. Buradi, S.A. Khan, Power plant energy predictions based on thermal factors using ridge and support vector regressor algorithms. *Energies* **14**, 7254 (2021). <https://doi.org/10.3390/en14217254>
54. Z. Said, P. Sharma, L. Syam Sundar, A. Afzal, C. Li, Synthesis, stability, thermophysical properties and AI approach for predictive modelling of Fe₃O₄ coated MWCNT hybrid nanofluids. *J. Mol. Liq.* **340**, 117291 (2021). <https://doi.org/10.1016/j.molliq.2021.117291>